TractEM: Fast Protocols for Whole Brain Deterministic Tractography-Based White Matter Atlas

Roza G. Bayrak[a,*], Kurt G. Schilling[b], Jasmine M. Greer[b], Colin B. Hansen[a], Christa M. Greer[b], Justin A. Blaber[c], Owen Williams[d], Lori L. Beason-Held[d], Susan M. Resnick[d], Baxter P. Rogers[b,e], Bennett A. Landman[a,b,c,e]

[a] *Computer Science, Vanderbilt University, Nashville TN, USA*
[b] *Vanderbilt University Institute of Imaging Science, Nashville TN, USA*
[c] *Electrical Engineering, Vanderbilt University, Nashville TN, USA*
[d] *Laboratory of Behavioral Neuroscience, National Institute on Aging, National Institutes of Health, Baltimore, MD, USA*
[e] *Department of Radiology and Radiological Sciences, Vanderbilt University, Nashville TN, USA*

Abstract

Reproducible identification of white matter tracts across subjects is essential for the study of structural connectivity of the human brain. One of the key challenges is anatomical differences between subjects. Labeling white matter regions of interest presents many challenges due to the need to integrate both local and global information. Clearly communicating the human/manual processes to capture this information is cumbersome, and the state-of-the-art for white matter atlas is the population-averaged Johns Hopkins Eve atlas. A critical bottleneck with the Eve atlas framework is that manual labeling time is extensive and peripheral white matter regions are conservatively labeled. In this work, we developed and tested a protocol for a simpler and flexible approach based on modern tractography definitions. The TractEM protocols for whole brain tractography take less than 6 hours for one subject. We tested the protocols on 61 unique tracts for 20 subjects manually labeled at least twice per subject. We analyzed reproducibility of the fiber bundles using volumetric overlap metrics, Dice correlation coefficient, continuous Dice correlation coefficient; distance metric, root mean squared error; and probabilistic intraclass correlation (ICC). Raters with minimal neuroanatomical expertise attained good and high reproducibility for typical 3T research resolution and high-resolution Human Connectome Project datasets, respectively. While the existing tractography methods tend to cover larger tracts and target only a limited number of tracts, the TractEM manual labeling protocols allow for reconstruction of reproducible region-specific fiber bundles across the brain. The protocols and sample results have been made available in open source.

Keywords: white matter atlas, structural connectivity, whole brain tractography, diffusion MRI, fast protocols

1. Introduction

Human brain atlases have had a transformative role in the study of neuroscience. Evolving neuroimaging, image processing, and analysis techniques are framing the way that we understand brain anatomy. Modern brain atlases (Mazziotta et al., 2001; Amunts et al., 2013; Hawrylycz et al., 2012) combine population atlases with multi-modal structural and functional information. These atlases provide a detailed representation of the anatomy and are a fundamental component of the field of image analysis. Although most commonly used modern approaches tend to treat white matter as essentially homogeneous, most current atlases are incomplete without detailed white matter information.

The effort to create atlases is not new. There is a wide range of existing study-specific atlases with varying modalities: structural and functional magnetic resonance imaging (MRI) (Bajcsy et al., 1983; Kikinis et al., 1996; Smith et al., 2004; Van Essen et al., 2011, 2012; Alivisatos et al., 2013), computed tomography (CT) (Bohm et al., 1983; Greitz et al., 1991; Salamon and Huang, 2012), multimodal atlases (Mega et al., 1997; Mazziotta et al., 2001; Schleicher et al., 2005); varying subjects: single atlases, population-based single atlases, multi-atlases (Lötjönen et al., 2010; Huo et al., 2016); varying image type schemes (Desikan et al., 2006), diffusion tensor imaging (Catani and De Schotten, 2008; Zhang and Arfanakis, 2018), histology (Talairach, 1988; Zilles and Amunts, 2010; Amunts et al., 2013; Mai et al., 2015), and even varying species (Youngren and Phillips, 1978; Dong, 2008; McLaren et al., 2009; Ramachandra and Subramanian, 2016; Reveley et al., 2016). Because white matter exhibits isointense signal on structural MRI, the structure is depicted as essentially homogeneous. Thus, there is a lack of atlases detailing white matter structure. White matter connectivity stores substantial information about functional neuroanatomy (Sporns et al.,

*Corresponding author
Email address: Roza.g.bayrak@vanderbilt.edu (Roza G. Bayrak)

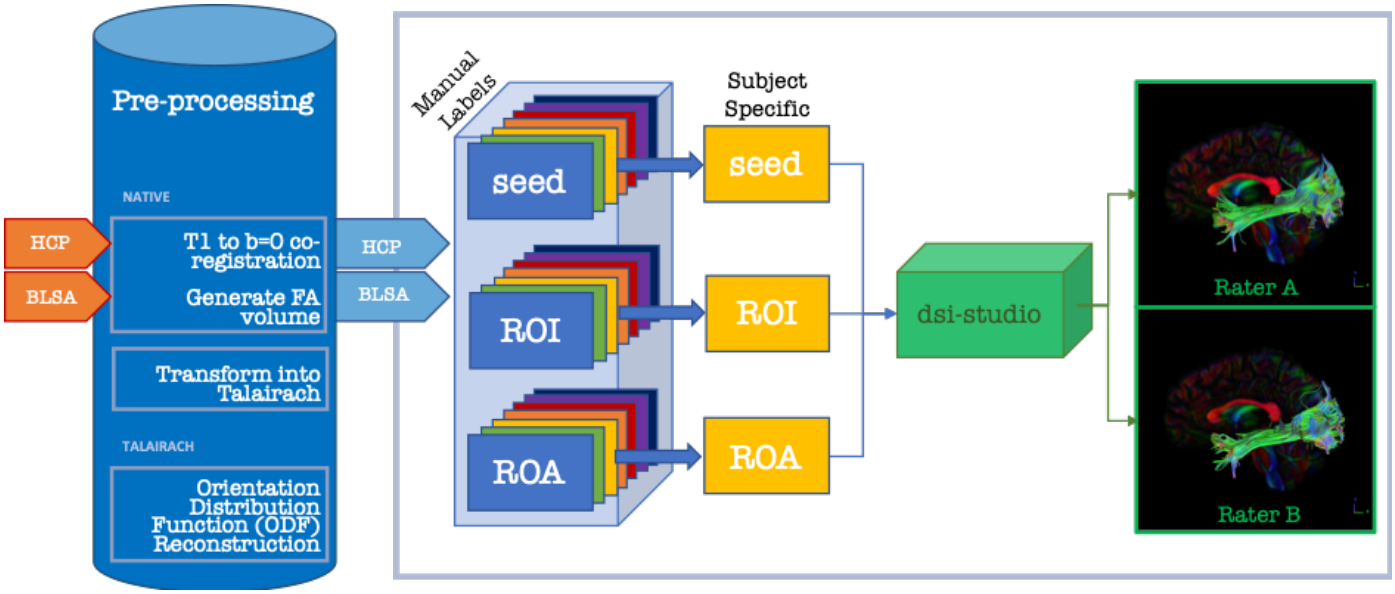

Figure 1: Pipeline overview: Pre-processing steps included susceptibility and eddy current corrections, and b0 signal normalization. A fractional anisotropy volume was created for every acquisition. After transferring each volume to Talairach space, 4th order spherical harmonic Q-ball imaging and generalized q-sampling are applied to BLSA and HCP datasets respectively to obtain orientation distribution functions, which are the inputs to DSI-Studio. The ODFs are used to create subject-specific 2D seed/ROI/ROA regions for each tract. Then region-based deterministic tractography is employed on the orientation maps. Each seed region was placed approximately in the middle of the bundle, all fibers entering the ROIs preserved and all passing through exclusion region (ROAs) masks are discarded. The results show two tractograms identified by different raters.

2005; Skudlarski et al., 2008; van den Heuvel et al., 2008; Greicius et al., 2009), longitudinal changes (Resnick et al., 2003), brain morphology (Lawes et al., 2008), abnormalities and their cognitive correlation (Gunning-Dixon and Raz, 2000), critical periods for neural development (Anderson et al., 2011), recovery and plasticity (Jiang et al., 2006; Dayan and Cohen, 2011), and cognitive functioning (Llinás et al., 1998). Nonetheless, existing white matter atlases are limited to population-averaged single atlases with extremely time consuming manual delineation (Mori et al., 2008), atlases lacking comprehensive coordinate information about white matter structures (Klingler and Gloor, 1960) or atlases targeting selective tracts instead of the whole-brain (Wakana et al., 2004; Oishi et al., 2008; Adluru et al., 2016; Besseling et al., 2012; Nath et al., 2018; Zhang and Arfanakis, 2018).

The current state-of-the-art white matter atlas is the population-averaged Johns Hopkins University (JHU) atlas (Mori et al., 2008; Oishi et al., 2008) labeled referring to Mori et al. (2005) and Wakana et al. (2004), using both diffusion tensor data and a T1-structural image of the brain. The JHU white matter atlases are based on diffusion weighted magnetic resonance imaging and subsequent diffusion tractography. Diffusion magnetic resonance imaging allows diffusion of water molecules to be visualized by sensitizing images in the direction of the field gradients. Diffusion tensor imaging uses this information to calculate anisotropy and therefore orientation information of the neural pathways. The JHU atlas defines 50 white matter parcellations slice by slice. Tractography can be performed by placing manual regions of interest. There are several limitations to the use of the Eve-based frameworks: (1) it is a population-averaged single atlas, (2) the peripheral white matter regions are conservatively labeled and (3) averaging over many people causes blurring of small pathways. Additionally, (4) the atlas was generated using diffusion tensor imaging, which has been shown to have limitations in crossing fiber and complex regions (Oouchi et al., 2007), whereas a number of more advanced techniques have been adopted by the neuroimaging community (Tuch, 2004; Descoteaux et al., 2007; Yeh et al., 2010). A whole-brain white matter (WM) atlas, for population-based atlases, labeled with equivalent methodologies, tools and protocols is therefore a fundamental resource for integrative and comprehensive modern brain atlases. In this work, we rectify the lack of available manually traced data for regional white matter definitions by developing a protocol informed by the Eve labeling scheme so that (1) all pathways can be manually traced in less than 6 hours, (2) using regions driven by current state-of-the art tractography, (3) with a methodology that can be applied generally to a large number of subjects. We developed and implemented a pipeline (see Figure 1) that

tracks 61 pathways. The protocols are tested on multiple datasets and are assessed for reproducibility.

This method will serve as a valuable tool for the neuroimaging community. Specifically, TractEM is composed of datasets that include real human acquisitions, along with careful manual selection and definitions of ground truth streamlines. These protocols define 61 unique pathways, on multiple subjects, processed multiple times, and provide not only white matter volumes (or labels), but also streamlines themselves, a feature not provided by other open sourced datasets (Wasserthal et al., 2018; Zhang et al., 2018). Thus, TractEM will show value in region identification, normalization, anatomical validation, and even development of machine learning based tracking strategies (Poulin et al., 2019).

This paper is organized as follows. Section 2 describes the pipeline and methodology for the construction of tracts. Section 3 presents the results of intra-subject inter-rater tract reproducibility, tract variability, and rater reproducibility. Section 4 is reserved for general specific discussion, while section 5 offers a conclusion.

2. Materials and Methods

2.1. Data and Acquisition

The protocol was developed on datasets obtained from the Baltimore Longitudinal Study of Aging (BLSA) (Ferrucci, 2008) and Human Connectome Project (HCP) (Van Essen et al., 2012).

The BLSA dataset used in this study contains 10 subjects with ages ranging between 57-77 years old. The data were acquired after informed consent under institutional review board and accessed in de-identified form. Each session included a T1-weighted structural MP-RAGE (number of slices = 170, voxel size = 1.0x1.0x1.2mm3, reconstruction matrix = 256x256, flip angle = 8 degrees and TR/TE = 6.5ms/3.1ms) and two diffusion acquisitions. Diffusion data were acquired with a 3D spin-echo diffusion-weighted EPI sequence (TR = 7454 ms; TE = 75 ms). Each acquisition consisted of an initial b0 and 32 diffusion weighted volumes all with the same b-value of 700 s/mm2 (number of slices = 170, voxel size = 0.81x0.81x2.2mm3, reconstruction matrix=320x320, flip angle = 90 degrees, acquisition matrix=116x115, field of view = 260x260mm). Susceptibility correction (Andersson et al., 2003), eddy current (Andersson and Sotiropoulos, 2016) correction techniques, and b0 signal normalization were applied to the diffusion data as a preprocessing step.

The HCP dataset used in this study contains 10 healthy subjects with no known history of neuropathological and psychiatric diseases, ages ranging between 26-36. Diffusion scans obtained from HCP contained structural volume sampled at the same resolution as the diffusion data, the diffusion weighting (b-values) for each volume, the diffusion direction (b-vectors) for each volume, preprocessed diffusion time series, brain mask in diffusion space, and the effects of gradient nonlinearities on the b-values and b-vectors for each voxel. Diffusion data were acquired with a 3D spin-echo diffusion weighted EPI sequence (TR = 5520 ms; TE = 89.50 ms). Each diffusion acquisition consisted of six b0 and 90 diffusion weighted volumes all with 3 shells of b=1000, 2000, and 3000s/mm2 interspersed with an approximately equal number of acquisitions on each shell within each run (number of slices = 111, voxel size = 1.25x1.25x1.25mm3, flip angle = 79 degrees, field of view = 210mm). Susceptibility correction and eddy current correction techniques were applied to the diffusion data as a preprocessing step.

2.2. DSI-Studio

DSI-Studio (http://dsi-studio.labsolver.org) is an end-user program for diffusion tensor image computation, region of interest (ROI)-based deterministic diffusion fiber tracking and 3D visualization. In this project, we have used DSI-Studio for both reconstruction and fiber tracking. Deterministic tractography is a maximum likelihood estimation approach for the fiber tracks, with high sensitivity parameters (high SNR, high anisotropy, small step size) generates reliable fiber pathway trajectories (Côté et al., 2013; Christidi et al., 2016). DSI-Studio adopts a generalized deterministic tracking algorithm that uses quantitative anisotropy (QA) to improve accuracy.

2.2.1. Regions

DSI-Studio is an ROI-based tractography tool. Regions are defined as a set of voxels stored of by their coordinates. There are three different types of regions to inform fiber tracking. Multiple regions in combination can be used to control tracking when identifying fine grained details or complicated white matter structures. For example, if the tract is large, multiple regions of interest along with tract-specific exclusion regions can be chosen to identify it. Regions can be defined either by hand drawing or created using a segmentation method. Example regions are shown in Figure 2.

Seed – Seed regions serve as starting points for the algorithm. A user labels seeding voxels which then are converted to starting points by the tracking algorithm. These starting points are at the subvoxel resolution to accommodate the algorithm. For example, a seed voxel placed at (1, 1, 1) will have subvoxel seeding placed within (0.5 1.5, 0.5 1.5, 0.5 1.5). Within the voxel region (0.5 1.5, 0.5 1.5,

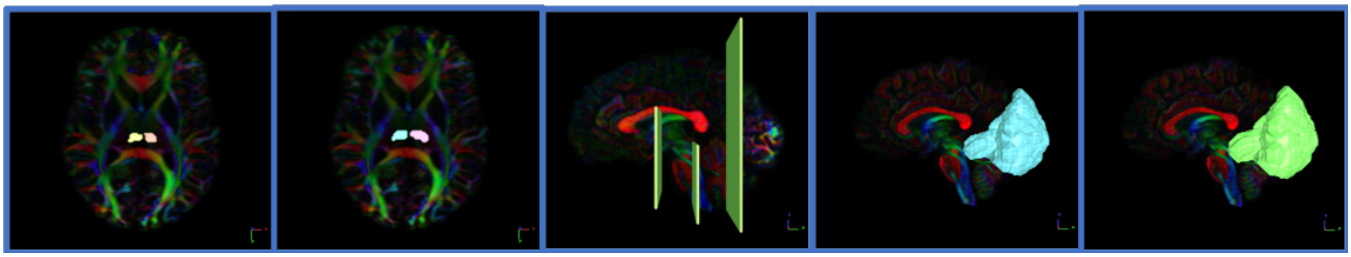

Figure 2: The regions for the region-based tractography that are used in TractEM are shown above (a) seed region, (b) ROI, (c), ROA, (d) 3D seed region, and (e) 3D end region (left to right).

0.5 1.5), DSI-Studio draws a point within the voxel range using a uniform distribution.

Region of interest (ROI) – These regions lead the fibers to where anatomical landmarks are. The streamlines are filtered in if passing through these landmarks, and eliminated from the tract if they are not.

Region of avoidance (ROA) – In the literature also commonly referred as NOT region or exclusion region. It is used to eliminate unwanted streamlines.

3D Seed Region – For this project, subject-specific 3D seed regions were segmented by a multi-atlas method (Asman and Landman, 2013). 3D seed regions define the starting points for the four lobes.

3D End Region – End region, as the name suggests, conserves only the tracts that end within a defined region. This is used for lobar region tracking. 3D end regions are created by dilating the multi-atlas segmented 3D seed regions for the same subject.

2.3. Pre-processing

The raw diffusion data were already corrected for head motion, eddy current effects, distortion (Van Essen et al., 2012), and b-table rotations (Schilling et al., 2019). When necessary T1 weighted images are co-registered to b=0. Using DSI-Studio, six elements tensor construction was performed on the diffusion-weighted image set to produce FA images in the subjects native space. The FA map was registered to a Talairach template image (Talairach, 1988) using an affine transformation. The template image was generated by applying an affine transformation of Lancaster et al. (2007) to the probabilistic ICBM152-space FA template image from the FSL atlas distribution (Mori et al., 2005; Wakana et al., 2007; Hua et al., 2008). The affine transformation was applied to the diffusion-weighted images, and the appropriate corresponding adjustment was made to the b-vectors.

For orientation distribution function (ODF), two high angular resolution diffusion imaging (HARDI) models for voxel-wise reconstruction were selected, according to the image quality of each datasets. HARDI models are capable of characterizing multiple directions and resolving crossing fiber issues (Tuch, 1999; Tuch et al., 2002; Descoteaux et al., 2007).

Q-ball Imaging (QBI) is the most commonly used reconstruction method. In this implementation, for the BLSA dataset, we fit 4th order spherical harmonic Q-ball. QBI uses a single shell (single b-value) to estimate the dODF to represent the fiber orientation distribution. DSI-Studio adopts the spherical harmonics based QBI reconstruction method by Descoteaux et al. (2007). For multi shell HCP data, generalized Q-sampling (GQI) reconstruction was used. GQI in addition to being capable of resolving crossing fiber issues, can utilize multi-shell (multi-b-value) data and works best with fairly dense sampling of directions to similarly estimate the dODF (Yeh et al., 2010).

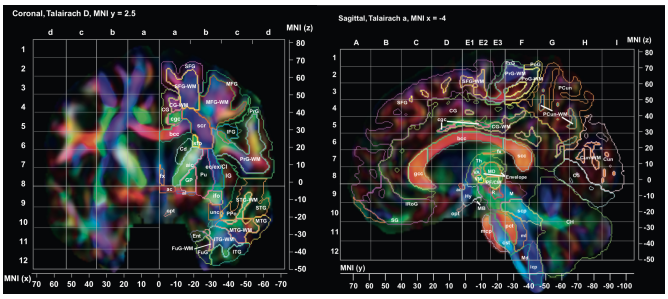

Figure 3: Region parcellations in Talairach from MRI atlas of human white matter used to develop TractEM protocol (a) coronal view of a random slice, (b) sagittal view of a near middle slice. Reprinted with the permission of Oishi et al., MRI atlas of human white matter, pg. 143 and pg. 249, Copyright Elsevier (2010).

2.4. Protocol Design

The protocols have been designed with reference to the Eve protocol (Oishi et al., 2010) whenever possible. Eve is an effective guide for region drawing with high inter-rater reproducibility (k > 0.85 and CoV < 3 %). A clear guide to a priori knowledge of the anatomy was prioritized

when defining the TractEM protocols. Example Eve white matter parcellation maps (WMPM) are shown in Figure 3. WMPM definitions are used to delineate tract-specific seed and ROI regions. 53 unique pathways, 22 of which have bilateral pairs of homologous tracts (22x2=44), 5 commissural pathways, 3 of the brainstem tracts and the optic tract were manually identified with Eve. In addition to the Eve-defined pathways, 8 subject-specific lobar regions were defined by a multi-atlas segmentation algorithm. A total of 61 fiber bundles were selected such that most of the brain was accounted for.

During the design and the development of the protocols, the high-acquisition (multi-shell) HCP dataset was used. Contrary to the Eve atlas, TractEM protocols do not divide anatomical fibers into multiple regions. Instead, anatomically consistent regions are merged into individual tracts. For the 53 Eve-defined pathways, seed regions were drawn roughly at the center of each tract. For bilateral tracts, seed regions were placed in both hemispheres. As white matter structural complexity increased, we increased the number of additional ROIs and ROAs in order to capture a tract as consistent as possible with its anatomical definition. In this manuscript, the complexity of the protocols is referred to as simple and complex tracts. If a protocol contains only a single seed region, e.g. genu of the corpus callosum (GCC), we refer it as a **simple tract**. If a protocol includes multiple combinations of seed/ROI/ROA, this is referred as a **complex tract**, e.g. inferior longitudinal fasciculus (ILF). For the lobar regions, multi-atlas segmented subject-specific 3D lobar masks were used as seed regions and 3x-dilated lobar masks were used as end regions. ROA regions were placed in order to isolate the tract or region of interest to fit into its anatomical definition for both the pathways and the lobes.

2.5. Application

2.5.1. Tracking Parameters

Tracking parameters were chosen carefully to reduce the number of false positive fibers and to ensure that the tracking does not suffer from premature termination. Parameters were termination index normalized QA (nqa), smoothing of 1, tract count of 100K, track length constraints 15-300 mm for lobar regions, and 30-300mm for the rest of the tracts. FA threshold of 0.1 is used to ensure the maximum number of fibers are produced. This is a suggested minimum as lower values may produce false fibers (http://dsi-studio.labsolver.org). Angular and FA thresholds are the determining parameters of how the fibers are tracked from the region of interest. Angular threshold is set to zero, therefore stopping criteria is not determined by this parameter; instead the length constraint or end regions serve as an end condition. The tracking algorithm is streamline (Euler), seed orientation is primary, and the direction interpolation is set to trilinear. Randomize seeding is off. This parameter sets the random seed generator to a constant to ensure tracking results are identical, and reproducible.

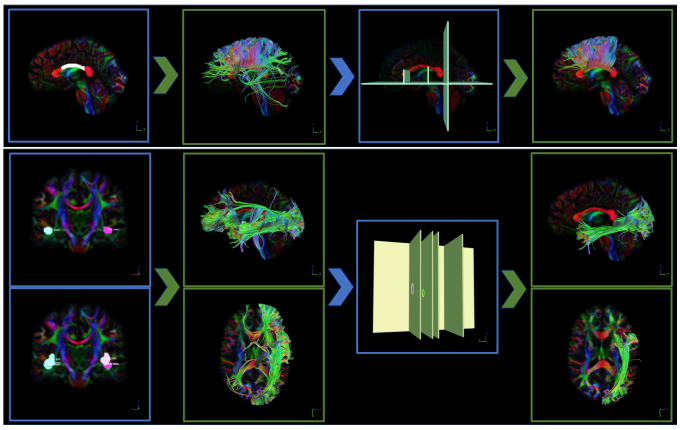

Figure 4: The application of TractEM on a simple (top) and a complex (bottom) tract. (a) Body of the corpus callosum is traced with a single seed region on the sagittal axis and one axial, three coronal ROA regions, (b) bilateral inferior longitudinal fasciculus is traced using one seed, two ROI regions for each side and multiple mutual ROA regions.

2.5.2. Fiber Tracking with DSI-Studio

The TractEM project (https://my.vanderbilt.edu/tractem) contains 35 tract specific protocols. Figure 4(a) is a visualization for the protocol of the body of corpus callosum. A sagittal seed region (at approx. sagittal slice 78) was created. The anterior extent of the seed region lines up with the most posterior part of the genu, whereas the posterior extent lines up with the most anterior part of the splenium. Then fiber tracking was executed. Based on the tracking output, 2-4 ROA regions were placed with one on an axial slice inferior to the seed regions, one on a coronal slice posterior to the seed region and when necessary a couple more on coronal slices inferior to the seed regions to control leakage into the fornix area. A second fiber tracking was then performed. The output was stored as streamlines (.trk) and converted into tract density maps (.nii) by counting the number of streamlines per voxel. Figure 4(b) depicts the protocol for inferior longitudinal fasciculus which required a more delineated protocol with multiple seed, ROI, and ROA regions. Lobar regions were traced using 3D regions. Subject-specific lobar masks were created using a multi-atlas segmentation algorithm applied to the T1 image in subjects native space. This segmentation was transformed to Talairach space using the affine transformation as defined in the pre-processing section.

2.5.3. Data Partitioning

The TractEM protocols are developed on 10 subjects from the high acquisition HCP dataset. The reproducibility testing of the protocols was made with an additional 10 subjects from the BLSA dataset, totaling 20 subjects. In order to test the reproducibility of the protocols, every subject has been traced at least two times by different raters.

3. Results

With the TractEM, we designed fast-tracking protocols that are driven by state-of-the-art tractography. Using the TractEM, we created a dataset that contains 2562 manually identified tracts. Fiber tracking for one subject took less than 6 hours with minimal neuroanatomical expertise required. Evaluation of the protocol was performed in 20 subjects where each subject was traced at least twice by different raters and reproducibility was assessed both qualitatively and quantitatively.

This section describes the evaluation procedure throughout the development and validation of the protocol. It is organized as follows. First, quality assessments were administered to check the validity of the tracts and approve/reject the methodology for the construction of tracts. Second, qualitative analyses demonstrated the resulting fiber tracts. Concluding analyses consisted of measures of inter-rater tract reliability, inter-subject variability, and intra-subject rater reproducibility.

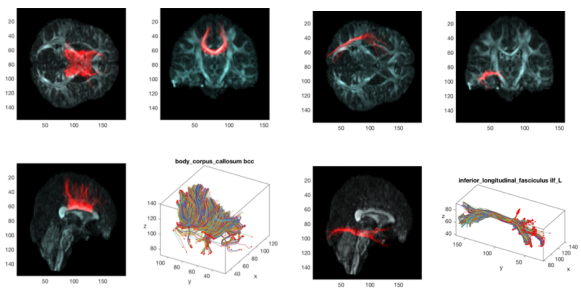

Figure 5: Axial, coronal, sagittal view of the density maps, and 3D visualization of streamlines for (a) body of the corpus callosum, and (b) inferior longitudinal fasciculus.

3.1. Quality Assessment

Quality assessment is a crucial step to ensure validity of tracts. We have prepared a performance analysis for immediate rater feedback. An automated pdf report is generated for each tract. It includes tract density visualization overlaid on the subjects FA images for all three views: sagittal, coronal, axial, and a 3D representation of the streamline Figure 5. This tool served as a quick visual sanity check to see if the assembled tract appears is consistent with the expected morphology. Initially, we used this assessment to improve the protocol. Its secondary and more important use is to check if the rater interpreted the protocol correctly.

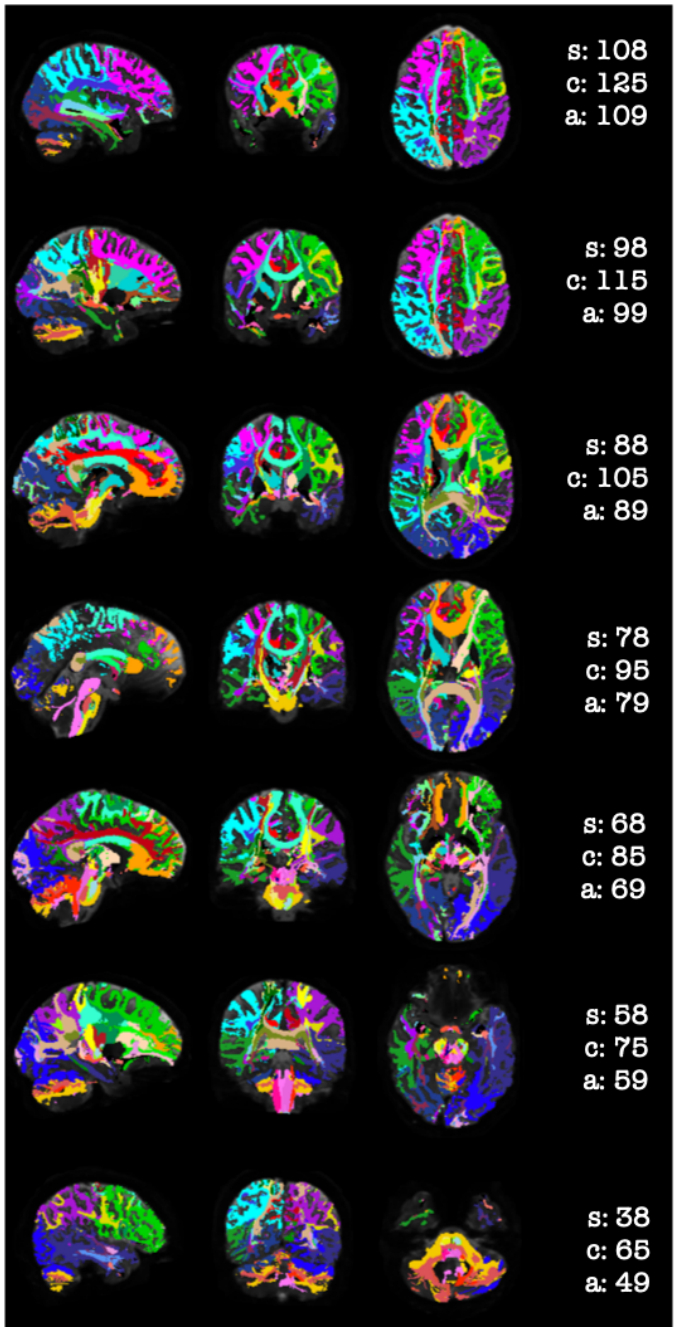

Figure 6: Tractography-based white matter atlas including 10 subjects total of 61 tracts with bilateral pairs is shown above from different slice views for all three views, sagittal (s), coronal (c), and axial (a), with slice numbers indicated.

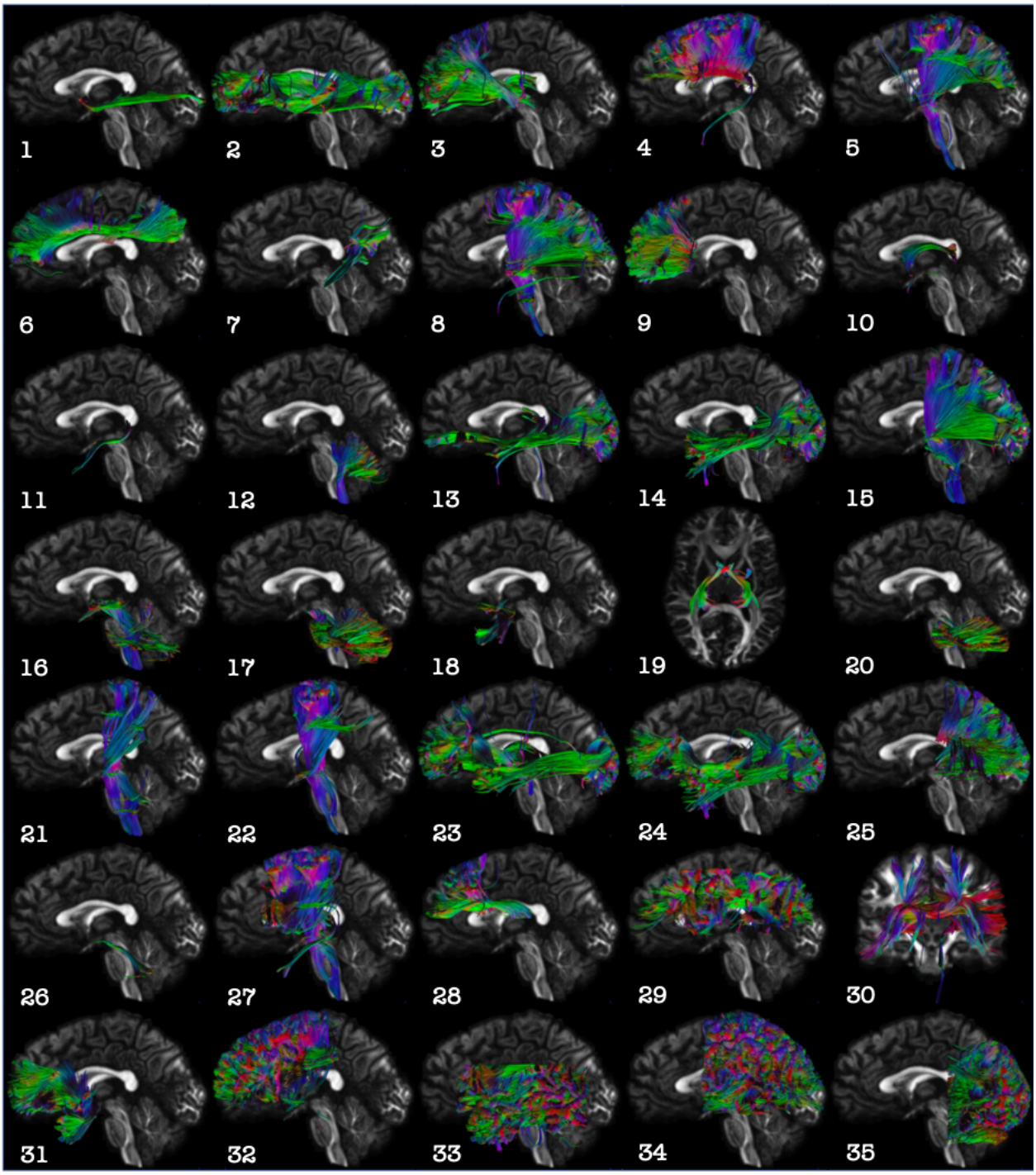

Figure 7: Complete protocol streamline visualization for a single HCP subject, (1) anterior commissure, (2) anterior corona radiata, (3) anterior limb internal capsule, (4) body corpus callosum, (5) cerebral peduncle, (6) cingulum cingulate gyrus, (7) cingulum hippocampal, (8) corticospinal tract, (9) fornix, (10)fornix stria terminalis, (11) genu corpus callosum, (12) inferior cerebellar peduncle, (13) inferior fronto-occipital fasciculus, (14) inferior longitudinal fasciculus, (15) medial lemniscus, (16) midbrain, (17) middle cerebellar peduncle, (18) olfactory radiation, (19) optic tract, (20) pontine crossing tract, (21) posterior corona radiata, (22) posterior limb internal capsule, (23) posterior thalamic radiation, (24) sagittal stratum, (25) splenium corpus callosum, (26) superior cerebellar peduncle, (27) superior corona radiata, (28) superior fronto-occipital fasciculus, (29) superior longitudinal fasciculus, (30) tapetum corpus callosum, (31) uncinate fasciculus, (32) frontal lobe, (33) temporal lobe, (34) parietal lobe, (35) occipital lobe.

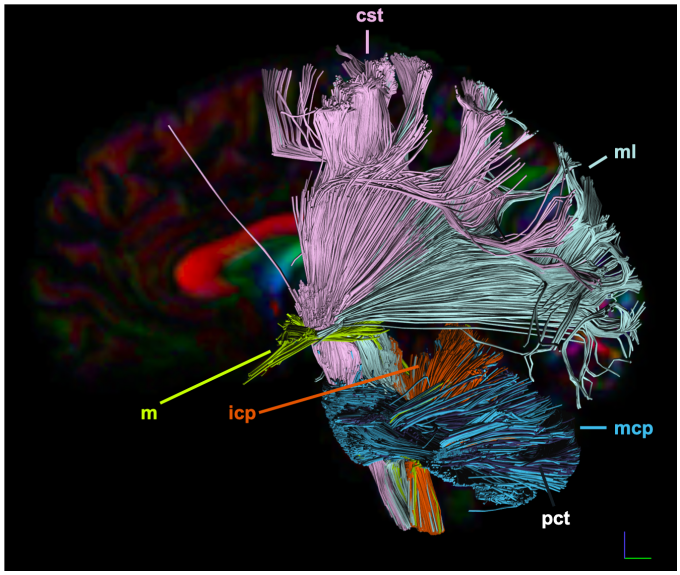

Figure 8: Tracts in the brainstem; corticospinal tract (CST), medial lemniscus (ML), midbrain (M), pontine crossing tract (PCT), inferior cerebellar peduncle (ICP), middle cerebellar peduncle (MCP), and superior cerebellar peduncle (SCP).

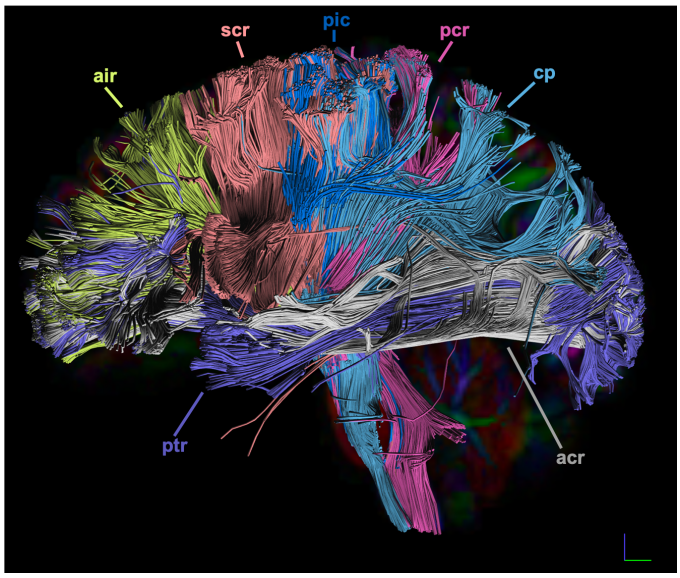

Figure 9: Projection fibers; anterior corona radiata (ACR), superior corona radiata (SCR), posterior corona radiata (PCR), posterior thalamic radiation (PTR), anterior limb of internal capsule (AIC), posterior limb of internal capsule (PIC), cerebral peduncle (CP).

3.2. Qualitative Analysis

Qualitative analysis is vital in order to contextualize the estimated fiber bundles. The characterization of individual fiber bundles can be inferred from these images, and the tracts can be investigated by their behavior (i.e. if the tract splits off from, is close to, integrates into another tract). Figure 6 shows the resulting averaged density maps of 61 white matter tracts for 20 subjects reconstructed using TractEM. Inter-regional relations and connections across the brain can be seen from these 3D fine detailed parcellation maps. Figure 7 demonstrates streamline representations of individual tracts for the all protocols for a single subject. Information about spatial location, shape, tract volume, proximity to the other tracts are important bases when assessing reproducibility. Thus, we also provide the tract visualizations in five structural categories (1) tracts in the brainstem (Figure 8), (2) projection fibers which connect cerebral cortex to the central regions and to the other end to spinal cord (Figure 9), (3) association fibers which connect different region of cerebral cortex (Figure 10), (4) commissural fibers which connect the two hemispheres (Figure 11), and (5) lobes which are the four main cortical divisions (Figure 12).

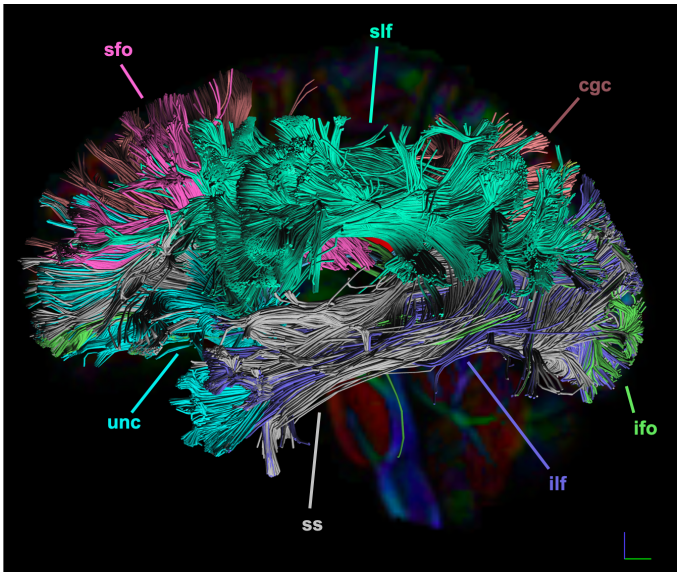

Figure 10: Association fibers; superior fronto-occipital fasciculus (SFO), inferior fronto-occipital fasciculus (IFO), superior longitudinal fasciculus (SLF), inferior longitudinal fasciculus (ILF), sagittal stratum (SS), uncinate fasciculus (UNC), cingulum cingulate gyrus (CGH).

3.3. Quantitative Analysis

Reproducibility analysis of the protocols is made possible by having white matter tracts of each subject traced by two separate raters. The protocols have been tested by ten raters who have no prior experience in tractography. Reproducibility was assessed between raters and across tracts. To measure the reliability of the protocols, we analyzed inter-rater tract reliability. We also assessed inter-subject variability to highlight anatomical differences between subjects and intra-subject rater reproducibility to confirm the robustness of the protocol.

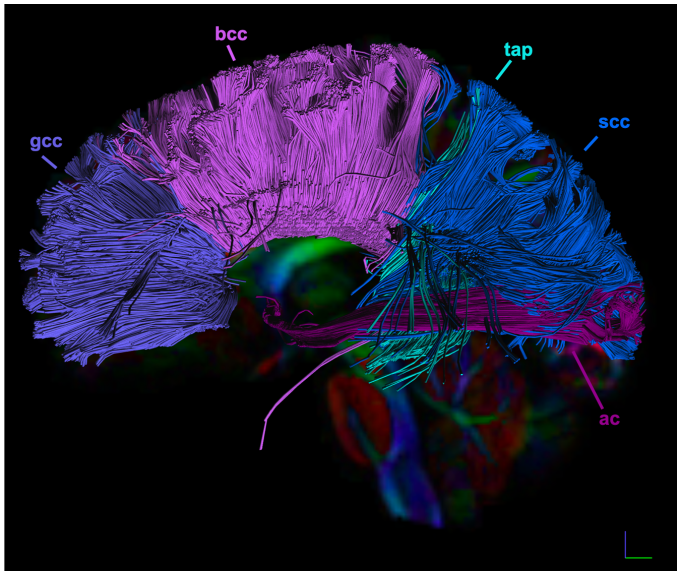

Figure 11: Commissural fibers; genu of the corpus callosum (GCC), body of the corpus callosum (BCC), splenium of the corpus callosum (SCC), and tapetum (TAP).

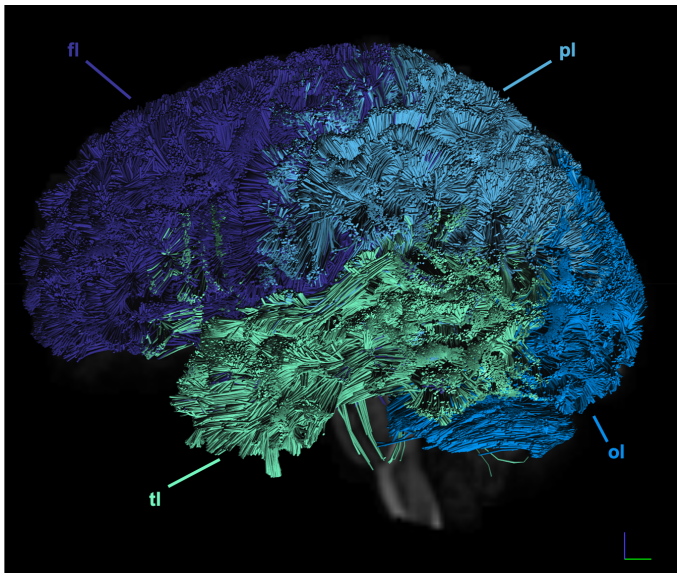

Figure 12: Commissural fibers; genu of the corpus callosum (GCC), body of the corpus callosum (BCC), splenium of the corpus callosum (SCC), and tapetum (TAP).

3.3.1. Inter-rater Tract Reliability

Same subject analysis leverages reproducibility analysis of a protocol by removing the anatomical variation. Intra-subject inter-rater tract reproducibility assessment was made by evaluating rater agreement for each tract. The score was calculated by averaging similarity across all subjects for a corresponding tract. Dice correlation coefficient (DICE), continuous DICE (cDICE), intra-class correlation (ICC) and root mean squared error (rMSE) metrics (see metrics in details in Appendix A) were used for the analysis. For each tract, medians and standard deviations were plotted for both datasets. HCP has shown cDICE (threshold = 0.05) > 0.85, ICC > 0.8 reproducibility on most tracts. BLSA results have shown cDICE (threshold = 0.05) > 0.7, ICC > 0.65 reproducibility for most tracts, which is lower than the HCP dataset. We defined the pathways during the TractEM development stage as lobar regions, simple and complex tracts. This description simply explains the type and number of regions used to track these pathways. Lobar regions were created using a multi-atlas segmentation method, simple tract protocols have one seed, and complex tract protocols are defined with the combination of 1+ seed and ROI regions. Lobar regions exhibit very high reproducibility across both datasets. Simple tracts showed generally higher reproducibility than more complex tracts. For simple tracts, even though HCP showed a more distinguishable division of reproducibility between simple and complex tracts, the BLSA dataset shows the same trend. The reproducibility for simple tracts in the HCP, cDICE scores (th = 0.05) ranged from very reproducible 0.95 to highly reproducible 0.7 and ICC scores fall into a similar scale between 0.98-0.68; for the BLSA, 0.88 > cDICE (th = 0.05) > 0.57, 0.94 > ICC > 0.3. The reproducibility of complex tracts in the HCP, cDICE (th = 0.05) scores ranged between 0.9 and 0.1 and ICC scores ranged between 0.95 and 0.1; for the BLSA, 0.83 > cDICE (th = 0.05) > 0.22 and 0.87 > ICC > 0.08.

The distribution of these tracts is detailed for the 61 unique tracts and for each error metric, it is shown in the form of box plots Appendix B, Figure B.1-10. In addition to the box plots, the mean and the standard deviation cDICE and ICC are averaged across hemispheres and provided in Appendix B, Table B.1 for precise numeric probing.

Inter-hemisphere asymmetry was observed even though the protocols were the same for the same tract. Bilaterality of white matter pathways has been reported in many previous studies in healthy subjects (Galaburda et al., 1978; Pujol et al., 2002; Park et al., 2004; Kanaan et al., 2012). The asymmetry suggested to occur during development, with age, in disease as well as it is observed between genders (Toga and Thompson, 2003). Bilateral reproducibility similarly varied more when the tract fell into the complex tract category.

3.3.2. Inter-subject Variability

Inter-subject variability was analyzed to understand anatomical variability across subjects. The variability is calculated by measuring the similarity between every subject for each dataset. To note that these analyses also have

the variability introduced from inter-rater reproducibility. Inter-subject variability is a crucial contributor to the reproducibility analyses of the tracts. This information is provided to aid a fair evaluation of the intra-subject tract reliability. The results have confirmed the variability (0.7 > cDICE, ICC) that rises from microstructural differences between subjects (Appendix B), Figure B.11-14.

3.3.3. Intra-subject Rater Reproducibility

The rater reproducibility evaluates the performance of different raters on images acquired under different acquisition parameters. A single rater tested all 35 protocols on their assigned subjects. Depending on their availability, the raters traced 1-5 subjects per person on each dataset (please see Table 1). On unanticipated occurrences, some raters traced the same-subject tract more than once. This issue was raised from failures in following the protocols. 67 tracts on BLSA data and only 2 tracts on HCP data were replaced and resulted in intra-rater pairs. These tracts were also included in the tract reliability analyses. Before the study, raters had neuroanatomical backgrounds ranging from no-knowledge to basic-knowledge. The results have shown homogeneity thus confirming the robustness of the protocols. For the multi-shell HCP dataset, the rater reproducibility was expectedly higher than the single-shell BLSA dataset. The overall rater reproducibility varied by less than 25% within each dataset. Evaluations across the five metrics are shown for both BLSA and HCP datasets in Appendix B, Figure B.15-16.

Dataset\Rater ID	R1	R2	R3	R4	R5	R6	R7	R8	R9	R10
BLSA	3	3	5	3	1	1	2	3	-	-
HCP	2	2	3	3	-	2	3	3	1	1

Table 1: Rater distributions are shown in the table for each dataset. The number in each box indicates the number of unique subjects that the raters traced. Each subject was traced at least 2 times for reproducibility analysis. For the BLSA dataset, total of 8 raters and for the HCP dataset, total of 9 raters tested the protocols.

4. General Discussion

The major advantage of diffusion tractography is that it provides reliable correspondence with white matter fiber pathways in vivo. Qualitative and quantitative identification of the estimated fiber pathways are crucial for the veracity of connectivity studies that rely on manual or automated approaches. Reproducible tractography can provide a backbone to the group-wise analyses and longitudinal testing studies for which a comprehensive modern atlas is essential. Despite the importance, there are a limited number of reproducibility studies with limited number of fiber pathways (Heiervang et al., 2006; Wakana et al., 2007; Besseling et al., 2012).

With the TractEM project, we tested 61 unique tracts using 35 protocols. The most reproducible fiber bundles were the lobar tracts, followed by corpus callosum (CC), cingulum, cerebral peduncle (CP), middle cerebral peduncle (MCP), corticospinal tract (CST), superior longitudinal fasciculus (SLF), inferior longitudinal fasciculus (ILF), inferior fronto-occipital fasciculus (IFO), and uncinate fasciculus (UNC) on both datasets. In contrast, FX, fornix stria-terminalis (FXST), superior cerebellar peduncle (SCP), posterior thalamic radiation (PTR) exhibited low reproducibility. These tracts fit in our complex tract description (please refer to Section 2.4). This shows that as the complexity of manual protocols increases, the rater reproducibility decreases. In addition to the complexity, manual region drawing and slice selection affected reproducibility. This reproducibility issue progressively improved as the protocol evolved by selecting easily identifiable parcels from Eve and adding specificity to the protocol descriptions such as approximated slice numbers.

As mentioned earlier, we assessed reproducibility on probabilistic density images. A direct comparison of the reproducibility could not be made between our analyses and ones in the literature due to the selection of different modalities and metrics. One of the earliest works on reproducible tractography is from Wakana et al. where they performed reproducibility analyses using kappa measure on FA and T2 for 11 tracts, 8 of which exist in TractEM (CGC, CGH, CST, SLF, ILF, IFO and UNC). The inter-institution inter-rater reproducibility is the closest assessment to our evaluation of tract reproducibility. These assessments resulted in average correlation ranging between 0.73-0.95 for the 8 tracts evaluated (Wakana et al., 2007). Heiervang et al. (2006) tested their most reproducible method of seed definition for probabilistic tractography. They evaluated tract volume overlap for only three TractEM corresponding tracts: cingulum bundle, GCC and optic radiation. Their results have shown inter-session and inter-subject mean overlap 81% and 50% respectively. Catani and De Schotten (2008) suggested a template guide for some of the association, projection and commissural pathways. They investigated cingulum, ILF, UNC, IFO, CC, AC, fornix (FX) and cerebral tracts and presented qualitative representations of them. The anatomical references are in agreement with our protocols. Another group, Besseling et al. (2012), did tract morphology similarity analyses for cingulum and GCC. They assessed reproducibility for proximal (excluding cortical projections) and extended (including cortical projections) streamlines.. The reproducibility of these two tracts was measured using DICE with a threshold of 5%. For the extended representation of cingulum and GCC, average DICE values were 0.82 and 0.84 respectively.

We have traced and analyzed lateral and single tracts that co-exist in both hemispheres. Our results quantitatively confirm the inter-hemisphere asymmetry that has been shown in multiple studies (Toga and Thompson, 2003; Wakana et al., 2007; de Schotten et al., 2011) (see Appendix B). It was not clear what caused this asymmetry, whether it was anisotropy or the size of the tracts. From a broader perspective, lateralization is evolutionary, hereditary, and developmental, and may occur as the result of disease. Mapping the asymmetry between hemispheres may be a very useful tool to identify abnormalities and the relationship between neighboring white matter tracts.

TractEM allows non-expert users to create whole brain tractography datasets. Using the protocol constructing a full dataset with 35 tracts with their bilateral counterparts is feasible (> 6 h/subject). To automate the protocol and create a multi-atlas, one may be able to deep learn tracking labels (seed, ROI, ROA etc.), anatomically consistent clearly defined pathways, and estimate streamlines. It also may be possible to directly learn tract density maps from FA maps or ODFs.

5. Conclusions

In this study, we addressed the lack of available manually traced data with a methodology driven by current state-of-the-art tractography that can be applied generally to large cohorts. In response to this challenge, we present the TractEM protocols. TractEM is an open source project, in terms of data and labeling guidelines. Comments and discussion are open for each tract. The frameworks enable versioning of tract definitions as consensus definitions evolve. By crowd sourcing our results, we aim to obtain expert validation for each tract. We made the sample data available which includes raw input data, Talairach aligned data, DSI-Studio ready input data, and TractEM results.

Acknowledgements.

This work was supported by the National Institutes of Health under award numbers R01EB017230, T32EB001628, and in part by ViSE/VICTR VR3029 and the National Center for Research Resources, Grant UL1 RR024975-01. This research was conducted with the support from Intramural Research Program, National Institute on Aging, NIH. The content is solely the responsibility of the authors and does not necessarily represent the official views of the NIH.

References

Adluru, N., Destiche, D. J., Tromp, D. P., Davidson, R. J., Zhang, H., Alexander, A. L., 2016. Evaluating consistency of deterministic streamline tractography in non-linearly warped dti data. arXiv preprint arXiv:1602.02117.

Alivisatos, A. P., Chun, M., Church, G. M., Deisseroth, K., Donoghue, J. P., Greenspan, R. J., McEuen, P. L., Roukes, M. L., Sejnowski, T. J., Weiss, P. S., et al., 2013. The brain activity map. Science 339 (6125), 1284–1285.

Amunts, K., Lepage, C., Borgeat, L., Mohlberg, H., Dickscheid, T., Rousseau, M.-É., Bludau, S., Bazin, P.-L., Lewis, L. B., Oros-Peusquens, A.-M., et al., 2013. Bigbrain: an ultrahigh-resolution 3d human brain model. Science 340 (6139), 1472–1475.

Anderson, V., Spencer-Smith, M., Wood, A., 2011. Do children really recover better? neurobehavioural plasticity after early brain insult. Brain 134 (8), 2197–2221.

Andersson, J. L., Skare, S., Ashburner, J., 2003. How to correct susceptibility distortions in spin-echo echo-planar images: application to diffusion tensor imaging. Neuroimage 20 (2), 870–888.

Andersson, J. L., Sotiropoulos, S. N., 2016. An integrated approach to correction for off-resonance effects and subject movement in diffusion mr imaging. Neuroimage 125, 1063–1078.

Asman, A. J., Landman, B. A., 2013. Non-local statistical label fusion for multi-atlas segmentation. Medical image analysis 17 (2), 194–208.

Bajcsy, R., Lieberson, R., Reivich, M., 1983. A computerized system for the elastic matching of deformed radiographic images to idealized atlas images. Journal of computer assisted tomography 7 (4), 618–625.

Besseling, R. M., Jansen, J. F., Overvliet, G. M., Vaessen, M. J., Braakman, H. M., Hofman, P. A., Aldenkamp, A. P., Backes, W. H., 2012. Tract specific reproducibility of tractography based morphology and diffusion metrics. PloS one 7 (4), e34125.

Bohm, C., Greitz, T., Kingsley, D., Berggren, B., Olsson, L., 1983. Adjustable computerized stereotaxic brain atlas for transmission and emission tomography. American Journal of Neuroradiology 4 (3), 731–733.

Catani, M., De Schotten, M. T., 2008. A diffusion tensor imaging tractography atlas for virtual in vivo dissections. cortex 44 (8), 1105–1132.

Christidi, F., Karavasilis, E., Samiotis, K., Bisdas, S., Papanikolaou, N., 2016. Fiber tracking: A qualitative and quantitative comparison between four different software tools on the reconstruction of major white matter tracts. European journal of radiology open 3, 153–161.

Côté, M.-A., Girard, G., Boré, A., Garyfallidis, E., Houde, J.-C., Descoteaux, M., 2013. Tractometer: towards validation of tractography pipelines. Medical image analysis 17 (7), 844–857.

Dayan, E., Cohen, L. G., 2011. Neuroplasticity subserving motor skill learning. Neuron 72 (3), 443–454.

de Schotten, M. T., Bizzi, A., Dell'Acqua, F., Allin, M., Walshe, M., Murray, R., Williams, S. C., Murphy, D. G., Catani, M., et al., 2011. Atlasing location, asymmetry and inter-subject variability of white matter tracts in the human brain with mr diffusion tractography. Neuroimage 54 (1), 49–59.

Descoteaux, M., Angelino, E., Fitzgibbons, S., Deriche, R., 2007. Regularized, fast, and robust analytical q-ball imaging. Magnetic Resonance in Medicine: An Official Journal of the International Society for Magnetic Resonance in Medicine 58 (3), 497–510.

Desikan, R. S., Ségonne, F., Fischl, B., Quinn, B. T., Dickerson, B. C., Blacker, D., Buckner, R. L., Dale, A. M., Maguire, R. P.,

Hyman, B. T., et al., 2006. An automated labeling system for subdividing the human cerebral cortex on mri scans into gyral based regions of interest. Neuroimage 31 (3), 968–980.

Dong, H. W., 2008. The Allen reference atlas: A digital color brain atlas of the C57Bl/6J male mouse. John Wiley & Sons Inc.

Ferrucci, L., 2008. The baltimore longitudinal study of aging (blsa): a 50-year-long journey and plans for the future.

Galaburda, A. M., LeMay, M., Kemper, T. L., Geschwind, N., 1978. Right-left asymmetrics in the brain. Science 199 (4331), 852–856.

Greicius, M. D., Supekar, K., Menon, V., Dougherty, R. F., 2009. Resting-state functional connectivity reflects structural connectivity in the default mode network. Cerebral cortex 19 (1), 72–78.

Greitz, T., Bohm, C., Holte, S., Eriksson, L., 1991. A computerized brain atlas: construction, anatomical content, and some applications. Journal of computer assisted tomography 15 (1), 26–38.

Gunning-Dixon, F. M., Raz, N., 2000. The cognitive correlates of white matter abnormalities in normal aging: a quantitative review. Neuropsychology 14 (2), 224.

Hawrylycz, M. J., Lein, E. S., Guillozet-Bongaarts, A. L., Shen, E. H., Ng, L., Miller, J. A., Van De Lagemaat, L. N., Smith, K. A., Ebbert, A., Riley, Z. L., et al., 2012. An anatomically comprehensive atlas of the adult human brain transcriptome. Nature 489 (7416), 391.

Heiervang, E., Behrens, T., Mackay, C., Robson, M., Johansen-Berg, H., 2006. Between session reproducibility and between subject variability of diffusion mr and tractography measures. Neuroimage 33 (3), 867–877.

Hua, K., Zhang, J., Wakana, S., Jiang, H., Li, X., Reich, D. S., Calabresi, P. A., Pekar, J. J., van Zijl, P. C., Mori, S., 2008. Tract probability maps in stereotaxic spaces: analyses of white matter anatomy and tract-specific quantification. Neuroimage 39 (1), 336–347.

Huo, Y., Plassard, A. J., Carass, A., Resnick, S. M., Pham, D. L., Prince, J. L., Landman, B. A., 2016. Consistent cortical reconstruction and multi-atlas brain segmentation. NeuroImage 138, 197–210.

Jiang, Q., Zhang, Z. G., Ding, G. L., Silver, B., Zhang, L., Meng, H., Lu, M., Pourabdillah-Nejed-D, S., Wang, L., Savant-Bhonsale, S., et al., 2006. Mri detects white matter reorganization after neural progenitor cell treatment of stroke. Neuroimage 32 (3), 1080–1089.

Kanaan, R. A., Allin, M., Picchioni, M., Barker, G. J., Daly, E., Shergill, S. S., Woolley, J., McGuire, P. K., 2012. Gender differences in white matter microstructure. PloS one 7 (6), e38272.

Kikinis, R., Shenton, M. E., Donnino, R. M., Jolesz, F. A., Iosifescu, D. V., McCarley, R. W., Saiviroonporn, P., Hokama, H. H., Robatino, A., Metcalf, D., et al., 1996. A digital brain atlas for surgical planning, model-driven segmentation, and teaching. IEEE Transactions on Visualization & Computer Graphics (3), 232–241.

Klingler, J., Gloor, P., 1960. The connections of the amygdala and of the anterior temporal cortex in the human brain. Journal of Comparative Neurology 115 (3), 333–369.

Lancaster, J. L., Tordesillas-Gutiérrez, D., Martinez, M., Salinas, F., Evans, A., Zilles, K., Mazziotta, J. C., Fox, P. T., 2007. Bias between mni and talairach coordinates analyzed using the icbm-152 brain template. Human brain mapping 28 (11), 1194–1205.

Lawes, I. N. C., Barrick, T. R., Murugam, V., Spierings, N., Evans, D. R., Song, M., Clark, C. A., 2008. Atlas-based segmentation of white matter tracts of the human brain using diffusion tensor tractography and comparison with classical dissection. Neuroimage 39 (1), 62–79.

Llinás, R., Ribary, U., Contreras, D., Pedroarena, C., 1998. The neuronal basis for consciousness. Philosophical Transactions of the Royal Society of London. Series B: Biological Sciences 353 (1377), 1841–1849.

Lötjönen, J. M., Wolz, R., Koikkalainen, J. R., Thurfjell, L., Waldemar, G., Soininen, H., Rueckert, D., Initiative, A. D. N., et al., 2010. Fast and robust multi-atlas segmentation of brain magnetic resonance images. Neuroimage 49 (3), 2352–2365.

Mai, J. K., Majtanik, M., Paxinos, G., 2015. Atlas of the human brain. Academic Press.

Mazziotta, J., Toga, A., Evans, A., Fox, P., Lancaster, J., Zilles, K., Woods, R., Paus, T., Simpson, G., Pike, B., et al., 2001. A probabilistic atlas and reference system for the human brain: International consortium for brain mapping (icbm). Philosophical Transactions of the Royal Society of London. Series B: Biological Sciences 356 (1412), 1293–1322.

McGraw, K. O., Wong, S. P., 1996. Forming inferences about some intraclass correlation coefficients. Psychological methods 1 (1), 30.

McLaren, D. G., Kosmatka, K. J., Oakes, T. R., Kroenke, C. D., Kohama, S. G., Matochik, J. A., Ingram, D. K., Johnson, S. C., 2009. A population-average mri-based atlas collection of the rhesus macaque. Neuroimage 45 (1), 52–59.

Mega, M. S., Chen, S. S., Thompson, P. M., Woods, R. P., Karaca, T. J., Tiwari, A., Vinters, H. V., Small, G. W., Toga, A. W., 1997. Mapping histology to metabolism: coregistration of stained whole-brain sections to premortem pet in alzheimer's disease. Neuroimage 5 (2), 147–153.

Mori, S., Oishi, K., Jiang, H., Jiang, L., Li, X., Akhter, K., Hua, K., Faria, A. V., Mahmood, A., Woods, R., et al., 2008. Stereotaxic white matter atlas based on diffusion tensor imaging in an icbm template. Neuroimage 40 (2), 570–582.

Mori, S., Wakana, S., Van Zijl, P. C., Nagae-Poetscher, L., 2005. MRI atlas of human white matter. Elsevier.

Nath, V., Schilling, K., Parvathaneni, P., Hainline, A. E., Huo, Y., Blaber, J. A., Rowe, M., Rodrigues, P., Prckovska, V., Aydogan, B., et al., 2018. Tractography reproducibility challenge with empirical data (traced): The 2017 ismrm diffusion study group challenge. BioRxiv, 484543.

Oishi, K., Faria, A. V., Van Zijl, P. C., Mori, S., 2010. MRI atlas of human white matter. Academic Press.

Oishi, K., Zilles, K., Amunts, K., Faria, A., Jiang, H., Li, X., Akhter, K., Hua, K., Woods, R., Toga, A. W., et al., 2008. Human brain white matter atlas: identification and assignment of common anatomical structures in superficial white matter. Neuroimage 43 (3), 447–457.

Oouchi, H., Yamada, K., Sakai, K., Kizu, O., Kubota, T., Ito, H., Nishimura, T., 2007. Diffusion anisotropy measurement of brain white matter is affected by voxel size: underestimation occurs in areas with crossing fibers. American Journal of Neuroradiology 28 (6), 1102–1106.

Park, H.-J., Westin, C.-F., Kubicki, M., Maier, S. E., Niznikiewicz, M., Baer, A., Frumin, M., Kikinis, R., Jolesz, F. A., McCarley, R. W., et al., 2004. White matter hemisphere asymmetries in healthy subjects and in schizophrenia: a diffusion tensor mri study. Neuroimage 23 (1), 213–223.

Poulin, P., Jörgens, D., Jodoin, P.-M., Descoteaux, M., 2019. Tractography and machine learning: Current state and open challenges. arXiv preprint arXiv:1902.05568.

Pujol, J., López-Sala, A., Deus, J., Cardoner, N., Sebastián-Gallés, N., Conesa, G., Capdevila, A., 2002. The lateral asymmetry of the human brain studied by volumetric magnetic resonance imaging. Neuroimage 17 (2), 670–679.

Ramachandra, R., Subramanian, T., 2016. Atlas of the neonatal rat brain. CRC press.

Resnick, S. M., Pham, D. L., Kraut, M. A., Zonderman, A. B., Davatzikos, C., 2003. Longitudinal magnetic resonance imaging studies of older adults: a shrinking brain. Journal of Neuroscience 23 (8), 3295–3301.

Reveley, C., Gruslys, A., Ye, F. Q., Glen, D., Samaha, J., E. Russ, B., Saad, Z., K. Seth, A., Leopold, D. A., Saleem, K. S., 2016. Three-dimensional digital template atlas of the macaque brain. Cerebral Cortex 27 (9), 4463–4477.

Salamon, G., Huang, Y. P., 2012. Computed tomography of the brain: atlas of normal anatomy. Springer Science & Business Media.

Schilling, K. G., Yeh, F.-C., Nath, V., Hansen, C., Williams, O., Resnick, S., Anderson, A. W., Landman, B. A., 2019. A fiber coherence index for quality control of b-table orientation in diffusion mri scans. Magnetic resonance imaging 58, 82–89.

Schleicher, A., Palomero-Gallagher, N., Morosan, P., Eickhoff, S., Kowalski, T., De Vos, K., Amunts, K., Zilles, K., 2005. Quantitative architectural analysis: a new approach to cortical mapping. Anatomy and embryology 210 (5-6), 373–386.

Shamir, R. R., Duchin, Y., Kim, J., Sapiro, G., Harel, N., 2018. Continuous dice coefficient: a method for evaluating probabilistic segmentations. BioRxiv, 306977.

Skudlarski, P., Jagannathan, K., Calhoun, V. D., Hampson, M., Skudlarska, B. A., Pearlson, G., 2008. Measuring brain connectivity: diffusion tensor imaging validates resting state temporal correlations. Neuroimage 43 (3), 554–561.

Smith, S. M., Jenkinson, M., Woolrich, M. W., Beckmann, C. F., Behrens, T. E., Johansen-Berg, H., Bannister, P. R., De Luca, M., Drobnjak, I., Flitney, D. E., et al., 2004. Advances in functional and structural mr image analysis and implementation as fsl. Neuroimage 23, S208–S219.

Sporns, O., Tononi, G., Kötter, R., 2005. The human connectome: a structural description of the human brain. PLoS computational biology 1 (4), e42.

Talairach, J., 1988. 3-dimensional proportional system; an approach to cerebral imaging. co-planar stereotaxic atlas of the human brain. Thieme, 1–122.

Toga, A. W., Thompson, P. M., 2003. Mapping brain asymmetry. Nature Reviews Neuroscience 4 (1), 37.

Tuch, D. S., 1999. High angular resolution diffusion imaging of the human brain. In: Proceedings of the 7th Annual Meeting of ISMRM, Philadelphia, 1999. Vol. 321.

Tuch, D. S., 2004. Q-ball imaging. Magnetic Resonance in Medicine: An Official Journal of the International Society for Magnetic Resonance in Medicine 52 (6), 1358–1372.

Tuch, D. S., Reese, T. G., Wiegell, M. R., Makris, N., Belliveau, J. W., Wedeen, V. J., 2002. High angular resolution diffusion imaging reveals intravoxel white matter fiber heterogeneity. Magnetic Resonance in Medicine: An Official Journal of the International Society for Magnetic Resonance in Medicine 48 (4), 577–582.

van den Heuvel, M., Mandl, R., Luigjes, J., Pol, H. H., 2008. Microstructural organization of the cingulum tract and the level of default mode functional connectivity. Journal of Neuroscience 28 (43), 10844–10851.

Van Essen, D. C., Glasser, M. F., Dierker, D. L., Harwell, J., Coalson, T., 2011. Parcellations and hemispheric asymmetries of human cerebral cortex analyzed on surface-based atlases. Cerebral cortex 22 (10), 2241–2262.

Van Essen, D. C., Ugurbil, K., Auerbach, E., Barch, D., Behrens, T., Bucholz, R., Chang, A., Chen, L., Corbetta, M., Curtiss, S. W., et al., 2012. The human connectome project: a data acquisition perspective. Neuroimage 62 (4), 2222–2231.

Wakana, S., Caprihan, A., Panzenboeck, M. M., Fallon, J. H., Perry, M., Gollub, R. L., Hua, K., Zhang, J., Jiang, H., Dubey, P., et al., 2007. Reproducibility of quantitative tractography methods applied to cerebral white matter. Neuroimage 36 (3), 630–644.

Wakana, S., Jiang, H., Nagae-Poetscher, L. M., Van Zijl, P. C., Mori, S., 2004. Fiber tract–based atlas of human white matter anatomy. Radiology 230 (1), 77–87.

Wasserthal, J., Neher, P., Maier-Hein, K. H., 2018. Tractseg-fast and accurate white matter tract segmentation. NeuroImage 183, 239–253.

Yeh, F.-C., Wedeen, V. J., Tseng, W.-Y. I., 2010. Generalized q-sampling imaging. IEEE transactions on medical imaging 29 (9), 1626–1635.

Youngren, O. M., Phillips, R. E., 1978. A stereotaxic atlas of the brain of the three-day-old domestic chick. Journal of Comparative Neurology 181 (3), 567–599.

Zhang, F., Savadjiev, P., Cai, W., Song, Y., Rathi, Y., Tunç, B., Parker, D., Kapur, T., Schultz, R. T., Makris, N., et al., 2018. Whole brain white matter connectivity analysis using machine learning: an application to autism. Neuroimage 172, 826–837.

Zhang, S., Arfanakis, K., 2018. Evaluation of standardized and study-specific diffusion tensor imaging templates of the adult human brain: Template characteristics, spatial normalization accuracy, and detection of small inter-group fa differences. Neuroimage 172, 40–50.

Zilles, K., Amunts, K., 2010. Centenary of brodmann's mapconception and fate. Nature Reviews Neuroscience 11 (2), 139.

Appendix A. Metrics For Quantitative Analysis

Appendix A.1. Metrics for Quantitative Analysis

We assessed reproducibility to test the TractEM protocols using Dice coefficient (DICE), Continuous Dice coefficient (cDICE), Intra-class correlation (ICC) and root mean squared error (rMSE). Reproducibility analysis is essential to validation of robustness. cDICE and ICC have been carefully chosen to fit the needs to describe our dataset. The reader should note that since we did not acquire ground truth for this study for every intra-subject comparison, one rater has randomly chosen from the pair and treated as ground truth.

Dice Correlation Coefficient

Dice correlation coefficient is a volumetric overlap metric. It quantifies binarized morphological similarity. Dice coefficient is defined as

$$Dice := \frac{2|A \cap B|}{|A| + |B|}, \tag{A.1}$$

where A and B represent binary images with values 0

and 1 for each voxel and computed as follows:

$$|A \cap B| = \sum_i a_i b_i, |A| = \sum_i a_i, |B| = \sum_i b_i. \quad \text{(A.2)}$$

Continuous Dice Correlation Coefficient

Continuous Dice coefficient (cDICE) (Shamir et al., 2018) is an alternative volumetric overlap metric to Dice coefficient (DICE). The major difference is that cDICE compares a ground truth binary image with a probabilistic map, which makes it suitable for probabilistic segmentation. cDICE is less dependent of the size of the structure and it accounts for partial volume effects which makes it less biased more robust. cDICE is defined as:

$$cDice := \frac{2|A \cap B|}{c|A| + |B|}, \quad \text{(A.3)}$$

where c defines the mean value of B over the voxels where both A and B positive numbers and computed as:

$$c = \frac{\sum_i a_i b_i}{\sum_i a_i sign(b_i)}, \quad \text{(A.4)}$$

where sign(x) is defined as:

$$sign(x) = \begin{cases} \text{1 if x} > 0 \\ \text{0 if x} = 0 \\ \text{-1 if x} < 0. \end{cases} \quad \text{(A.5)}$$

A is the binarized image with threshold = 0.05, B is the probabilistic map that is not thresholded. Two novelties in comparison to classic Dice coefficient, (1) cDICE is =1 if-and-only-if the structures overlap almost perfectly, (2) the score is monotonically decreasing with the amount of overlap.

Intraclass Correlation

The interclass correlation coefficient (ICC) (McGraw and Wong, 1996) is a measure of correlations between pairs of observations that do not necessarily have an order, or have obvious labels. It is common to use the ICC as a measure of agreement among observers; in our case it is used as a measure of agreement between two segmentations. Inter-class correlation is defined as

$$ICC = \frac{1}{Ns^2} \sum_{n=1}^{N} (x_{n,1} - \tilde{x})(x_{n,2} - \tilde{x}), \quad \text{(A.6)}$$

where

$$\tilde{x} = \frac{1}{2N} \sum_{n=1}^{N} (x_{n,1})(x_{n,2}), \quad \text{(A.7)}$$

$$s^2 = \frac{1}{2N} \left\{ \sum_{n=1}^{N} (x_{n,1} - \tilde{x}) + \sum_{n=1}^{N} (x_{n,2} - \tilde{x}) \right\} \quad \text{(A.8)}$$

Appendix B. Qualitative and Quantitative Representations of Results

This section is reserved for supplemental figures.

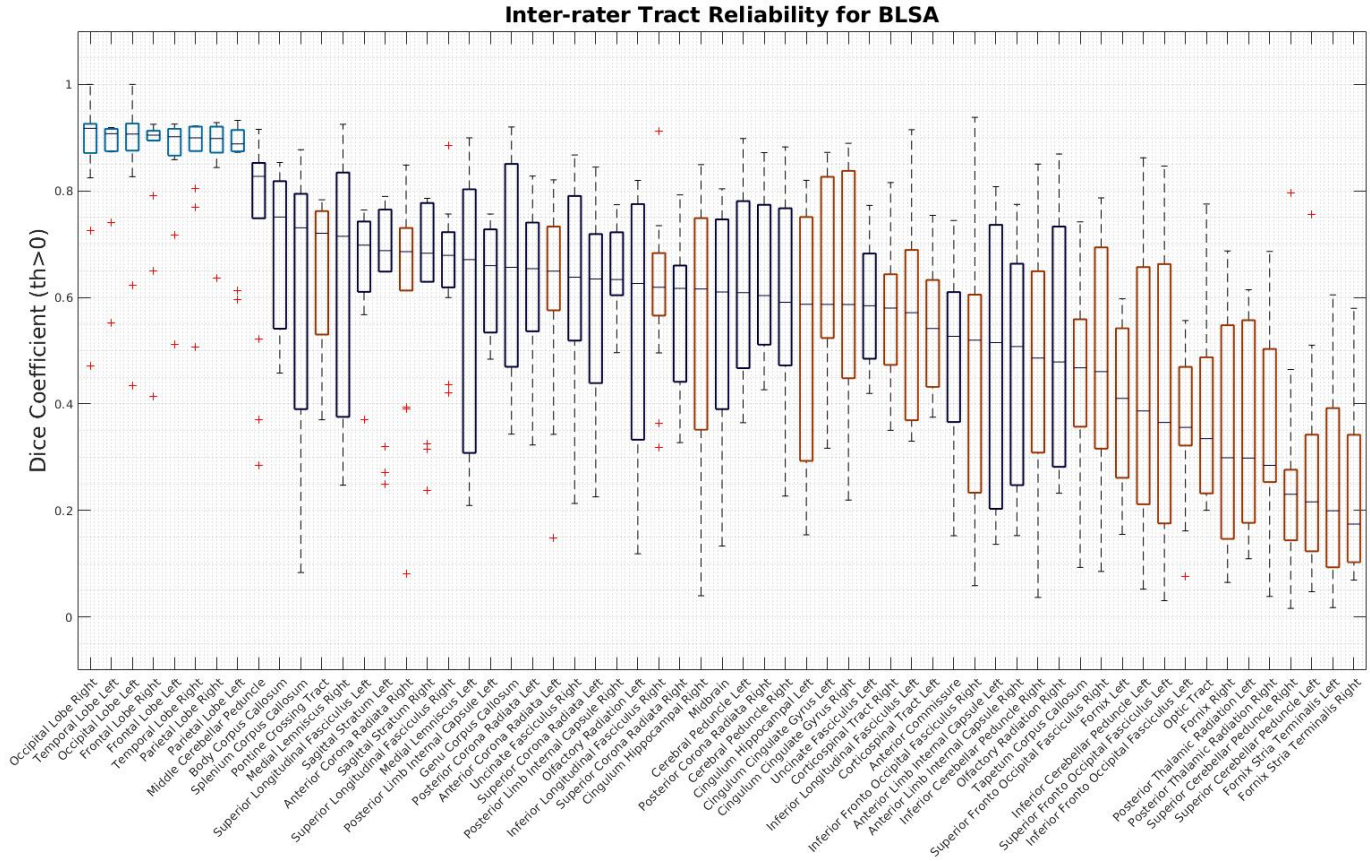

Figure B.1: TractEM tract reliability for all 61 fiber bundles is shown. Density images were binarized with a threshold > 0 for similarity analysis and similarity was calculated using Dice correlation coefficient. Each boxplot represents the similarity of same-subject different-rater pairs for 10 subjects from the BLSA dataset (see Section 3.3 Inter-rater Tract Reliability for the exceptions). The tracts are sorted from high to low reproducibility. Lobar regions are demonstrated with turquoise color, simple tracts are shown in dark blue, and complex tracts are represented by orange (see Section 2.4 TractEM Protocol Design for tract group descriptions).

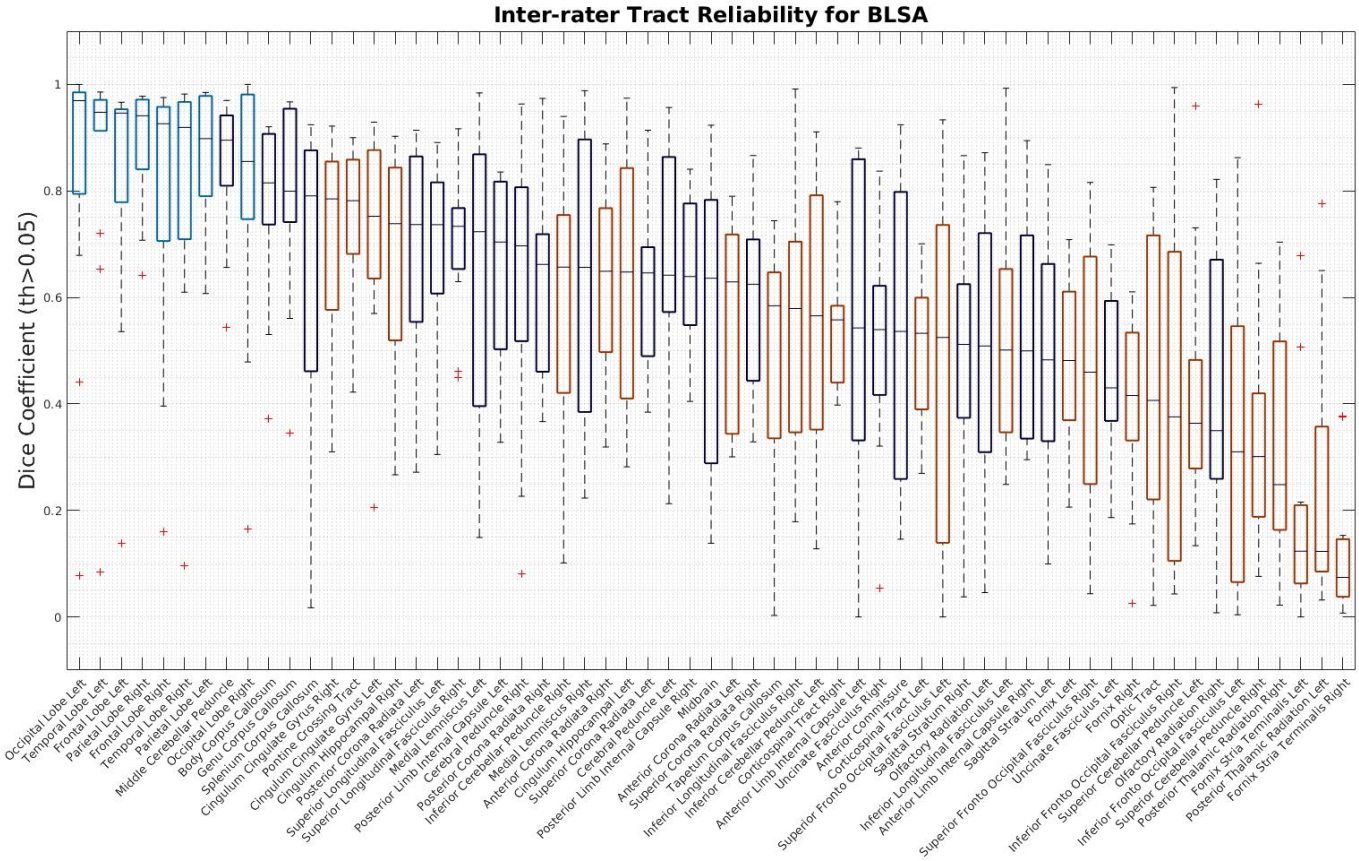

Figure B.2: TractEM tract reliability for all 61 fiber bundles is shown. Density images were binarized with a threshold > 0.05 for similarity analysis and similarity was calculated using Dice correlation coefficient. Each boxplot represents the similarity of same-subject different-rater pairs for 10 subjects from the BLSA dataset (see Section 3.3 Inter-rater Tract Reliability for the exceptions). The tracts are sorted from high to low reproducibility. Lobar regions are demonstrated with turquoise color, simple tracts are shown in dark blue, and complex tracts are represented by orange (see Section 2.4 TractEM Protocol Design for tract group descriptions).

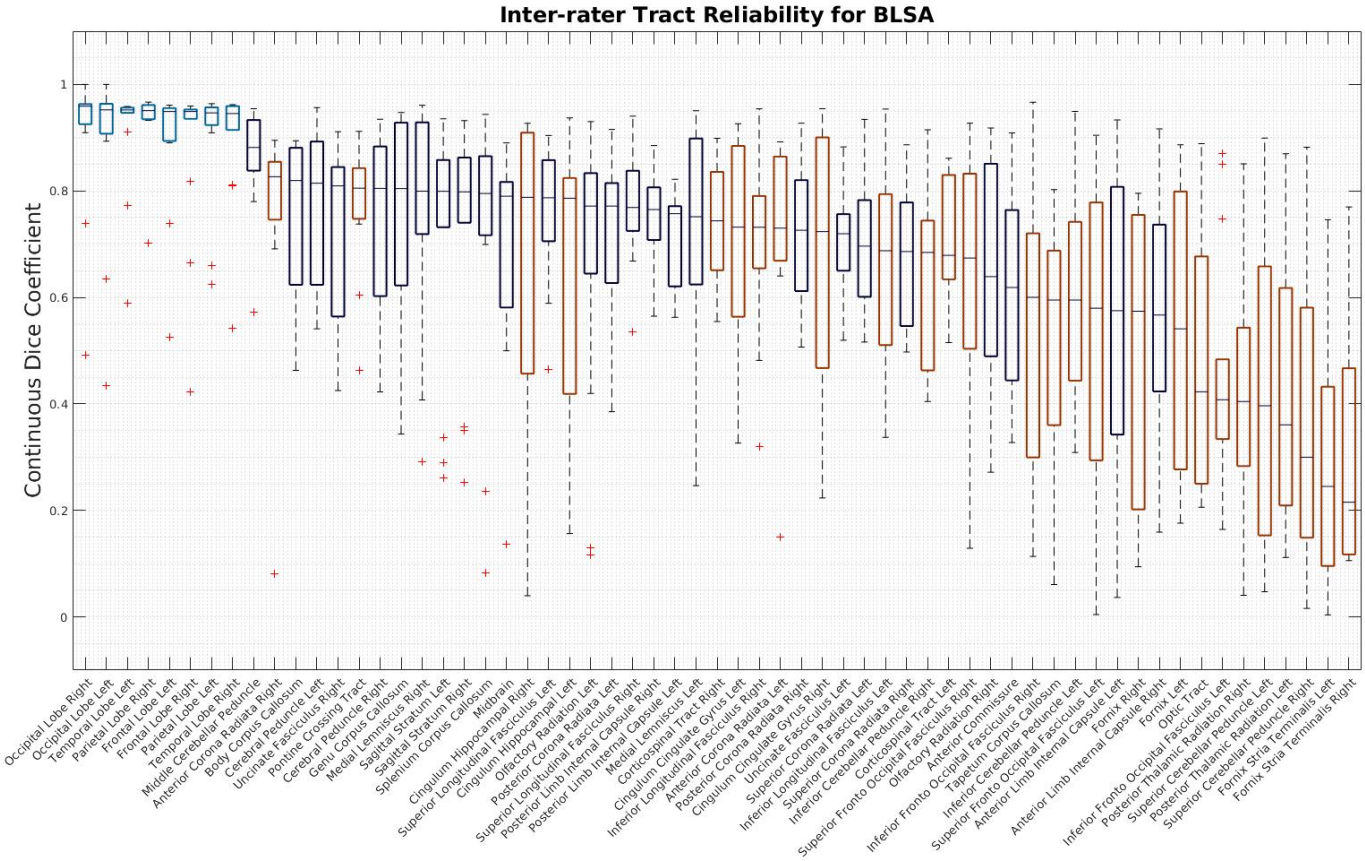

Figure B.3: TractEM tract reliability for all 61 fiber bundles is shown. Each data point on the boxplots represents the similarity of same-subject different-rater pairs for 10 subjects from the BLSA dataset (see Section 3.3 Inter-rater Tract Reliability for the exceptions). Similarity was calculated using continuous Dice correlation coefficient. One of the density images for each pair was binarized with a threshold > 0.05 for the analysis. The tracts are sorted from high to low reproducibility. Lobar regions are demonstrated with turquoise color, simple tracts are shown in dark blue, and complex tracts are represented by orange (see Section 2.4 TractEM Protocol Design for tract group descriptions).

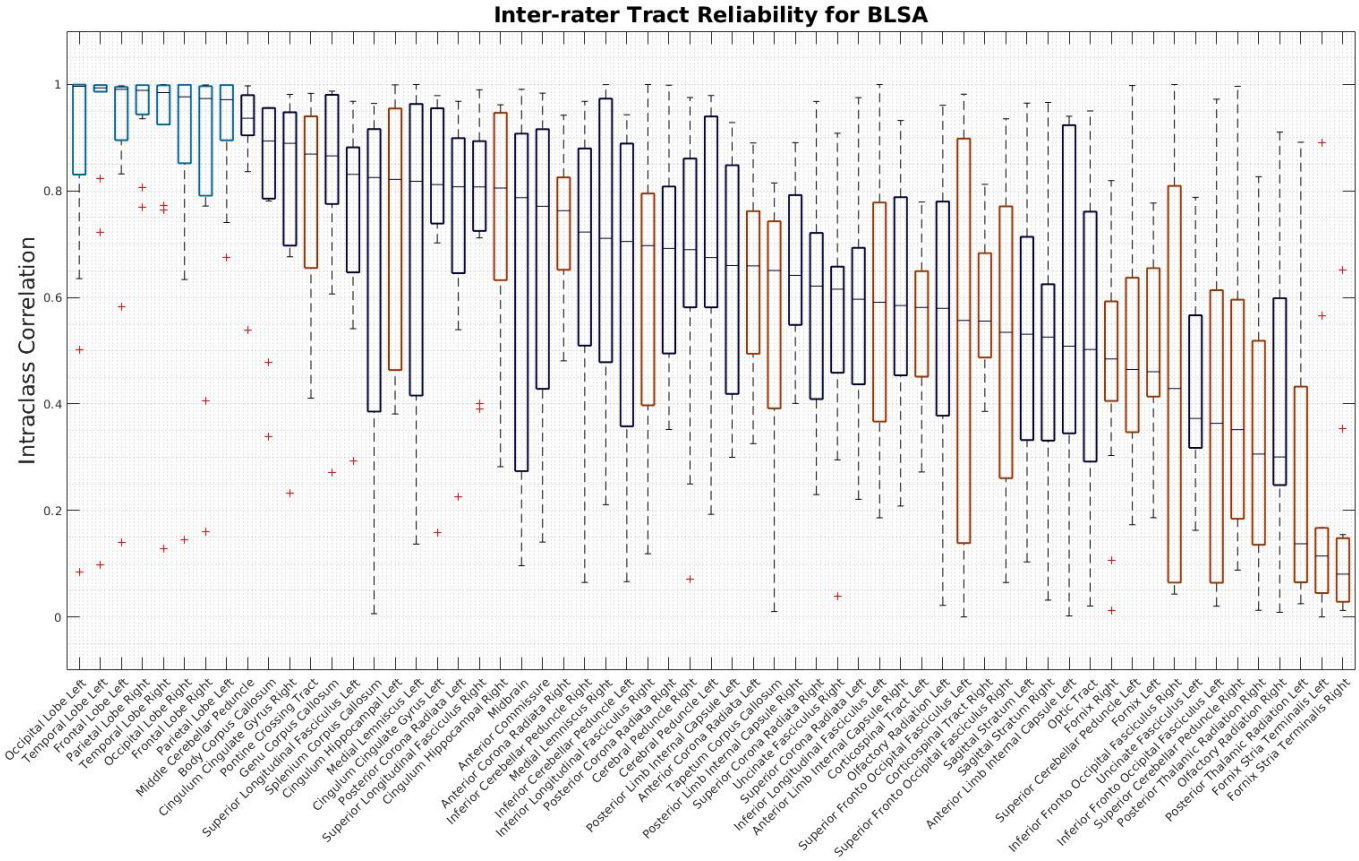

Figure B.4: TractEM tract reliability for all 61 fiber bundles is shown. Density images were used for similarity analysis and similarity was calculated using intraclass correlation coefficient. Each boxplot represents the similarity of same-subject different-rater pairs for 10 subjects from the BLSA dataset (see Section 3.3 Inter-rater Tract Reliability for the exceptions). The tracts are sorted from high to low reproducibility. Lobar regions are demonstrated with turquoise color, simple tracts are shown in dark blue, and complex tracts are represented by orange (see Section 2.4 TractEM Protocol Design for tract group descriptions).

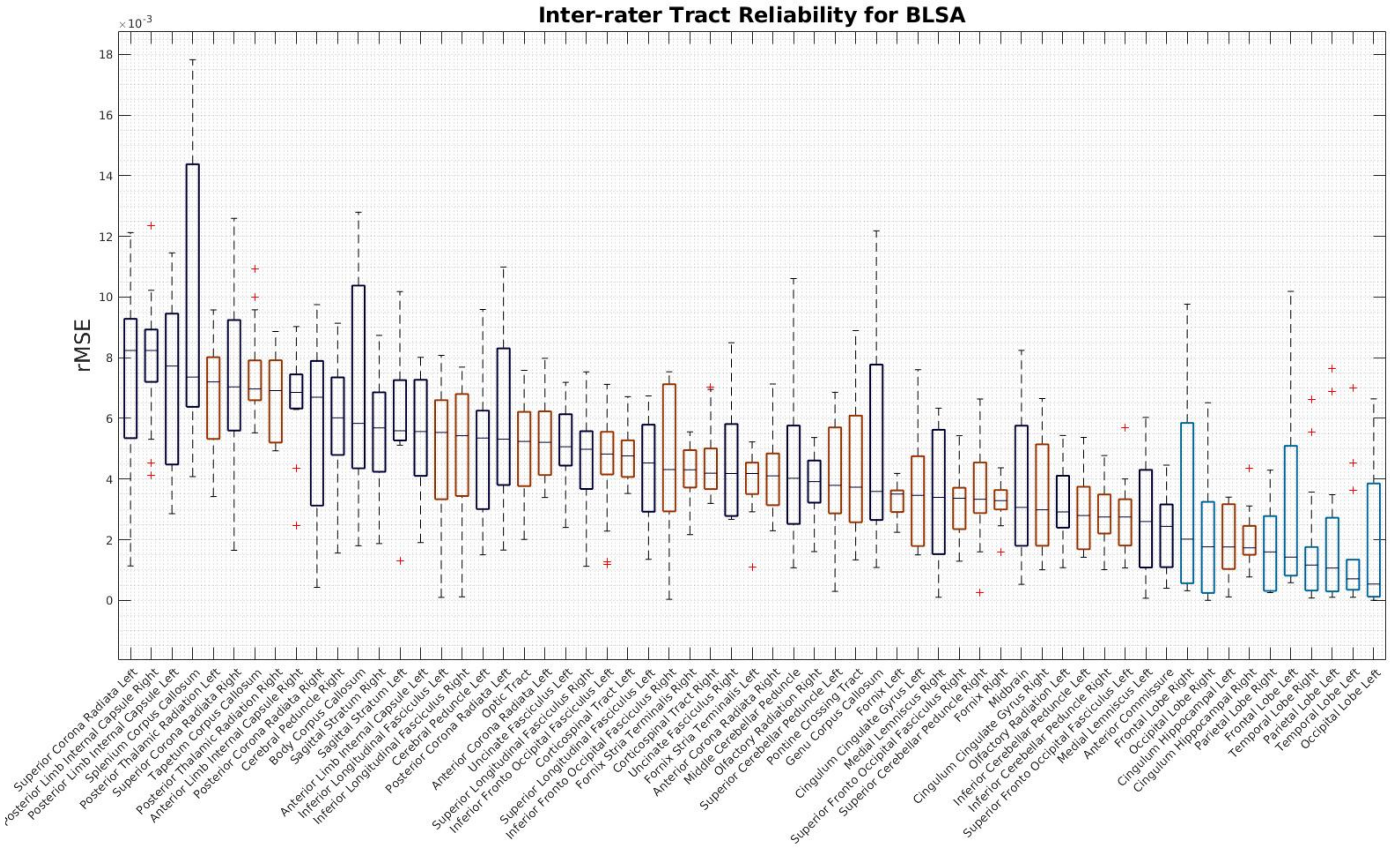

Figure B.5: TractEM tract reliability for all 61 fiber bundles is shown. Density images used for similarity analysis and similarity was calculated using root mean squared error. Each boxplot represents the similarity of same-subject different-rater pairs for 10 subjects from the BLSA dataset (see Section 3.3 Inter-rater Tract Reliability for the exceptions). The tracts are sorted from high to low reproducibility. Lobar regions are demonstrated with turquoise color, simple tracts are shown in dark blue, and complex tracts are represented by orange (see Section 2.4 TractEM Protocol Design for tract group descriptions).

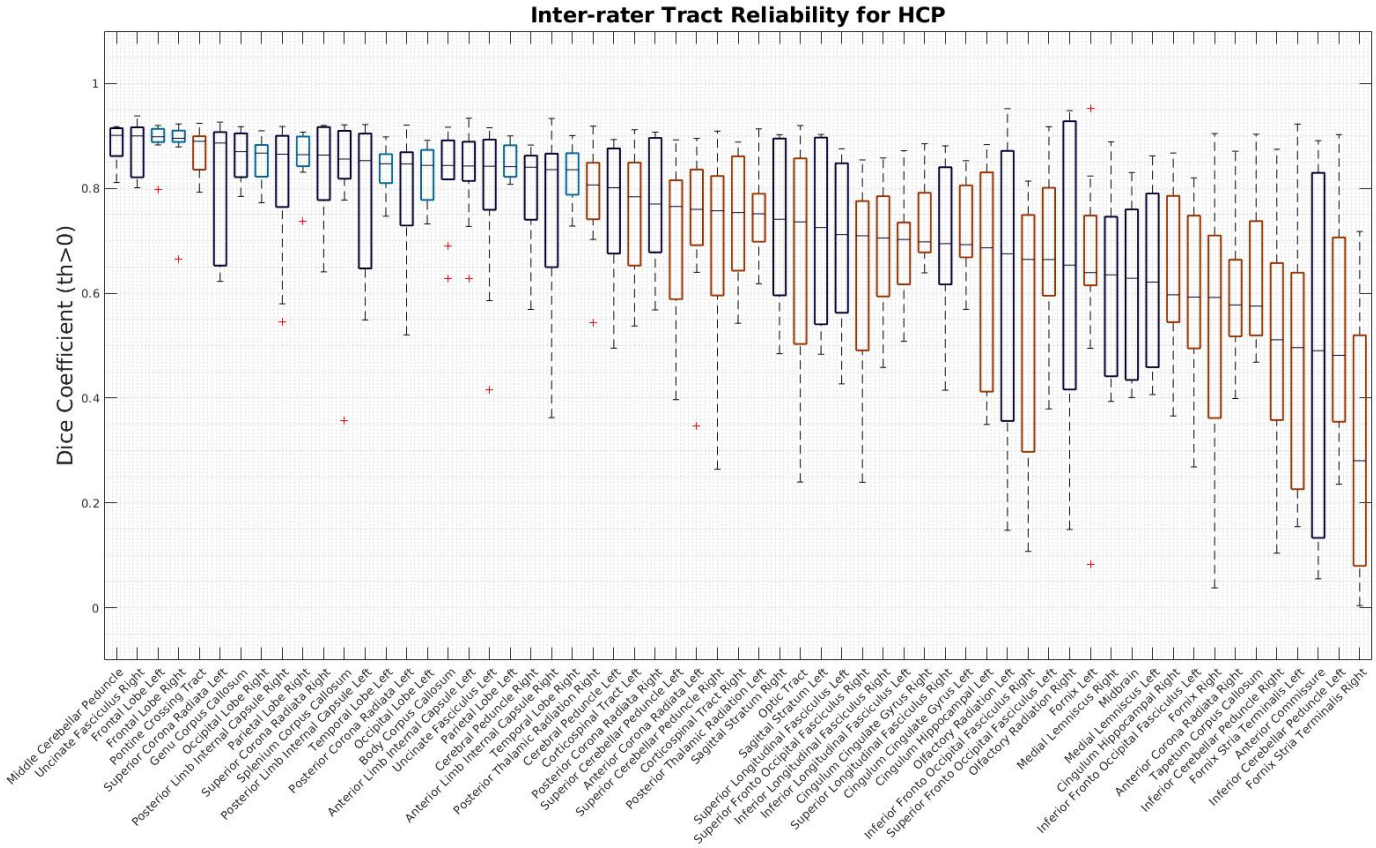

Figure B.6: TractEM tract reliability for all 61 fiber bundles is shown. Density images were binarized with a threshold > 0 for similarity analysis and similarity was calculated using Dice correlation coefficient. Each boxplot represents the similarity of same-subject different-rater pairs for 10 subjects from the HCP dataset (see Section 3.3 Inter-rater Tract Reliability for the exceptions). The tracts are sorted from high to low reproducibility. Lobar regions are demonstrated with turquoise color, simple tracts are shown in dark blue, and complex tracts are represented by orange (see Section 2.4 TractEM Protocol Design for tract group descriptions).

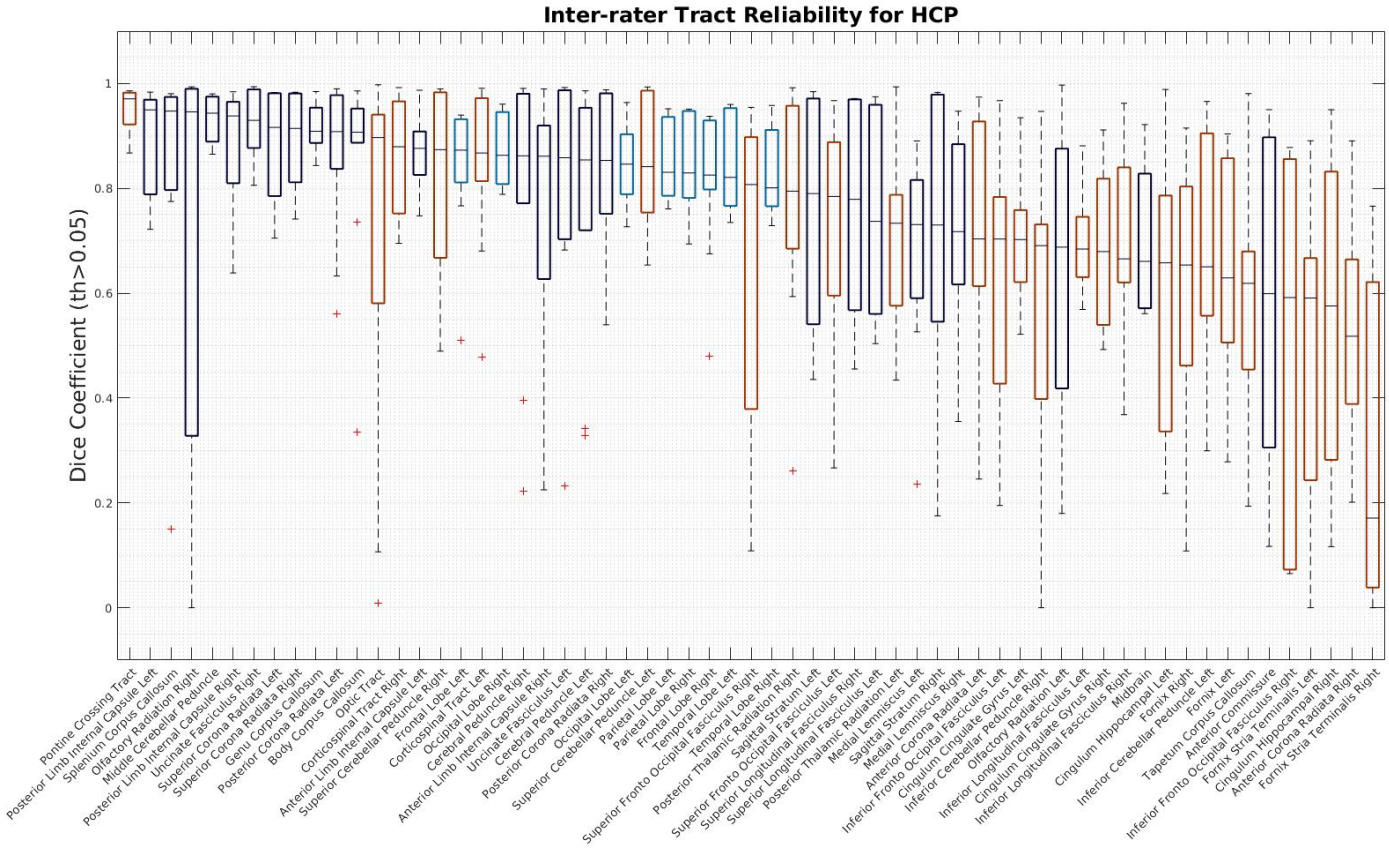

Figure B.7: TractEM tract reliability for all 61 fiber bundles is shown. Density images were binarized with a threshold > 0.05 for similarity analysis and similarity was calculated using Dice correlation coefficient. Each boxplot represents the similarity of same-subject different-rater pairs for 10 subjects from the HCP dataset (see Section 3.3 Inter-rater Tract Reliability for the exceptions). The tracts are sorted from high to low reproducibility. Lobar regions are demonstrated with turquoise color, simple tracts are shown in dark blue, and complex tracts are represented by orange (see Section 2.4 TractEM Protocol Design for tract group descriptions).

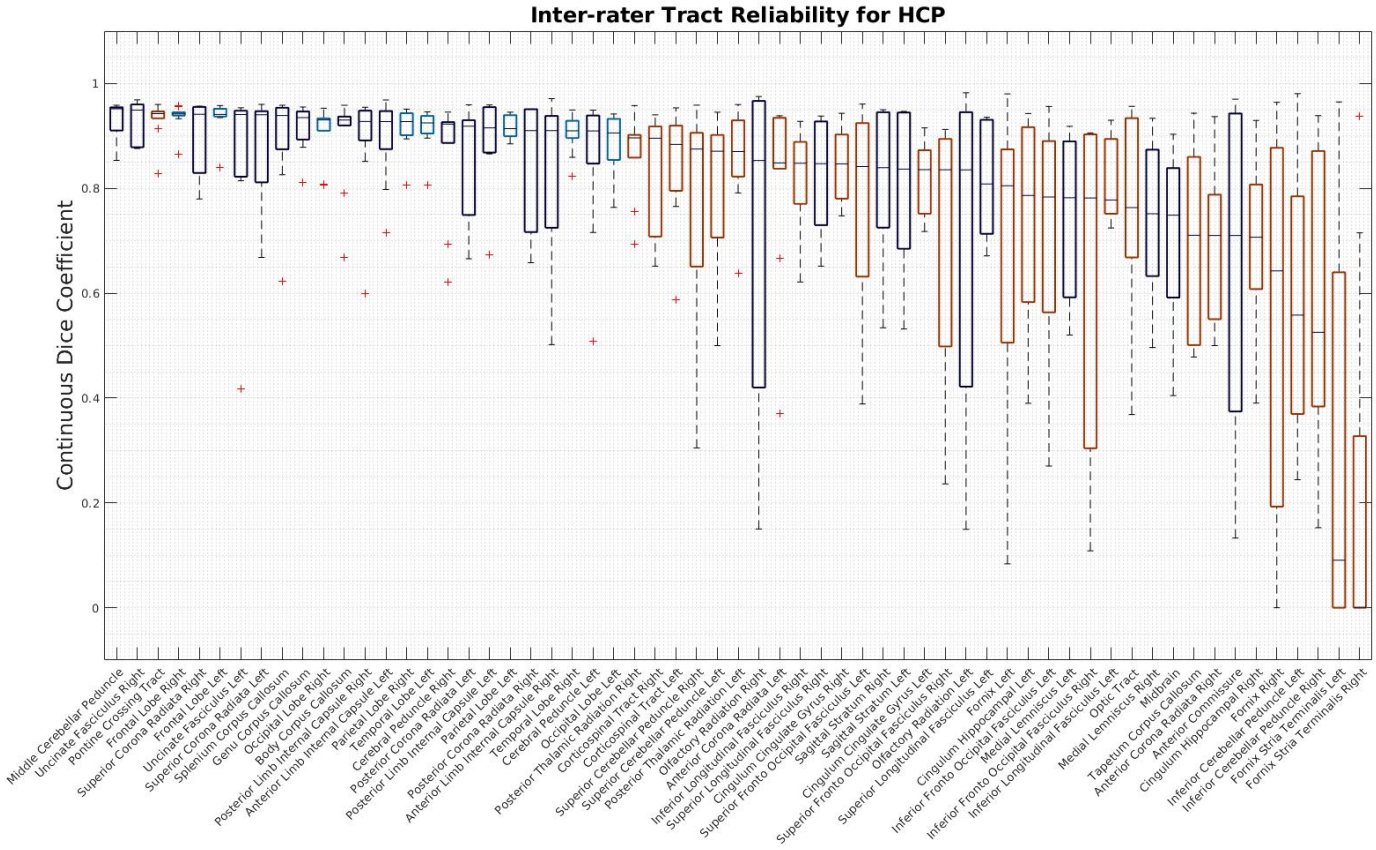

Figure B.8: TractEM tract reliability for all 61 fiber bundles is shown. Each data point on the boxplots represents the similarity of same-subject different-rater pairs for 10 subjects from the HCP dataset (see Section 3.3 Inter-rater Tract Reliability for the exceptions). Similarity was calculated using continuous Dice correlation coefficient. One of the density images for each pair was binarized with a threshold > 0.05 for the analysis. The tracts are sorted from high to low reproducibility. Lobar regions are demonstrated with turquoise color, simple tracts are shown in dark blue, and complex tracts are represented by orange (see Section 2.4 TractEM Protocol Design for tract group descriptions).

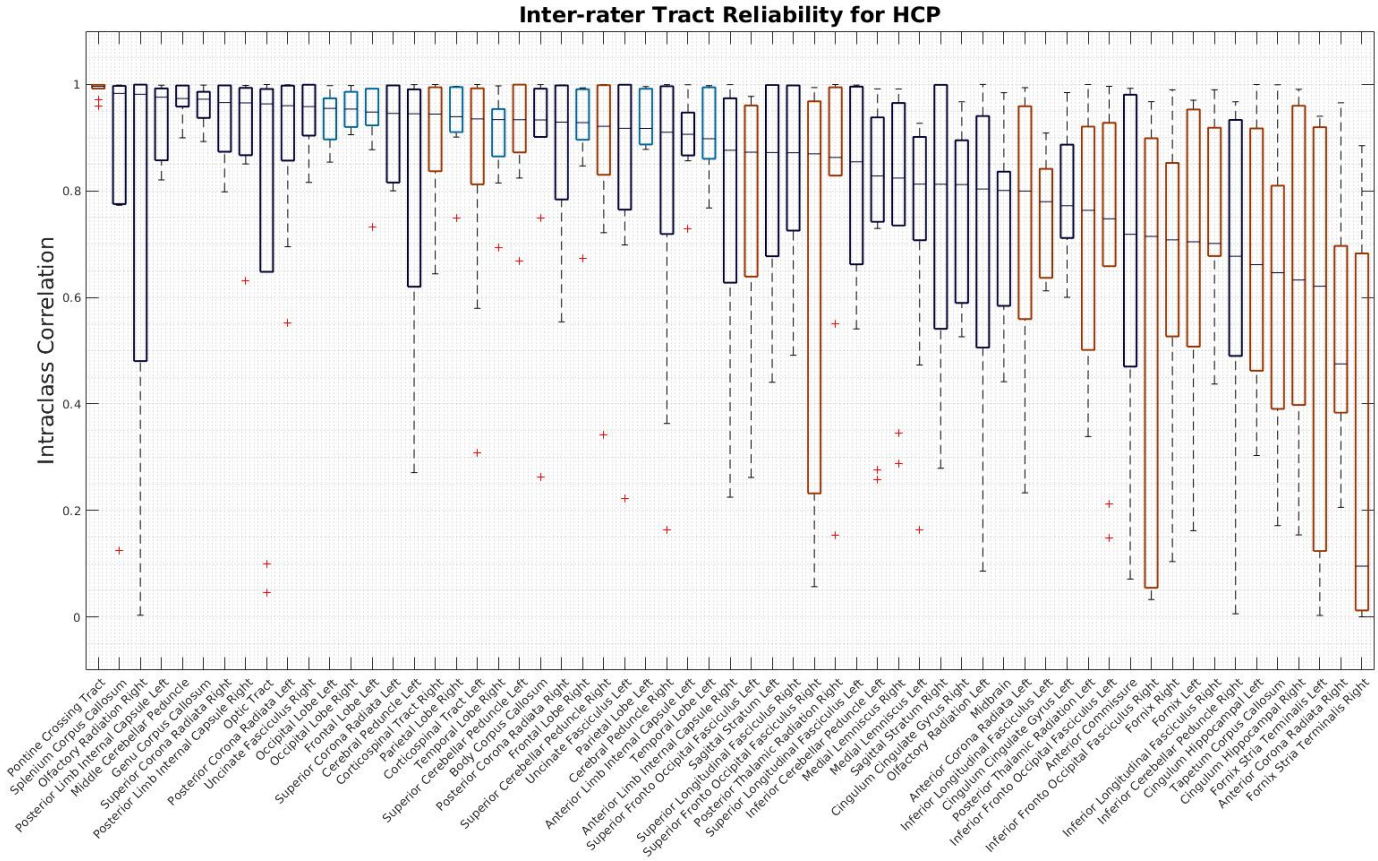

Figure B.9: TractEM tract reliability for all 61 fiber bundles is shown. Density images were used for similarity analysis and similarity was calculated using intraclass correlation coefficient. Each boxplot represents the similarity of same-subject different-rater pairs for 10 subjects from the HCP dataset (see Section 3.3 Inter-rater Tract Reliability for the exceptions). The tracts are sorted from high to low reproducibility. Lobar regions are demonstrated with turquoise color, simple tracts are shown in dark blue, and complex tracts are represented by orange (see Section 2.4 TractEM Protocol Design for tract group descriptions).

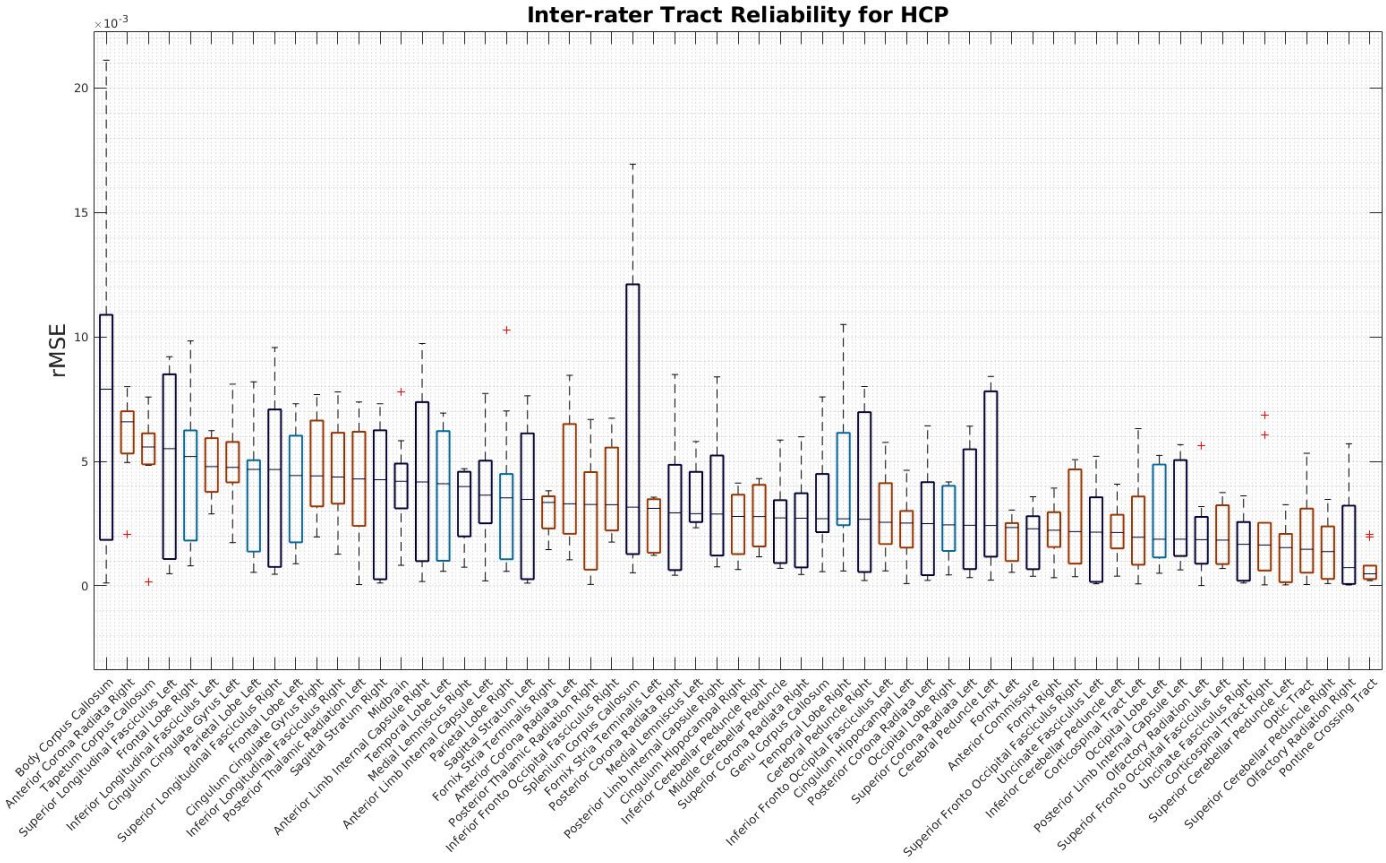

Figure B.10: TractEM tract reliability for all 61 fiber bundles is shown. Density images used for similarity analysis and similarity was calculated using root mean squared error. Each boxplot represents the similarity of same-subject different-rater pairs for 10 subjects from the HCP dataset (see Section 3.3 Inter-rater Tract Reliability for the exceptions). The tracts are sorted from high to low reproducibility. Lobar regions are demonstrated with turquoise color, simple tracts are shown in dark blue, and complex tracts are represented by orange (see Section 2.4 TractEM Protocol Design for tract group descriptions).

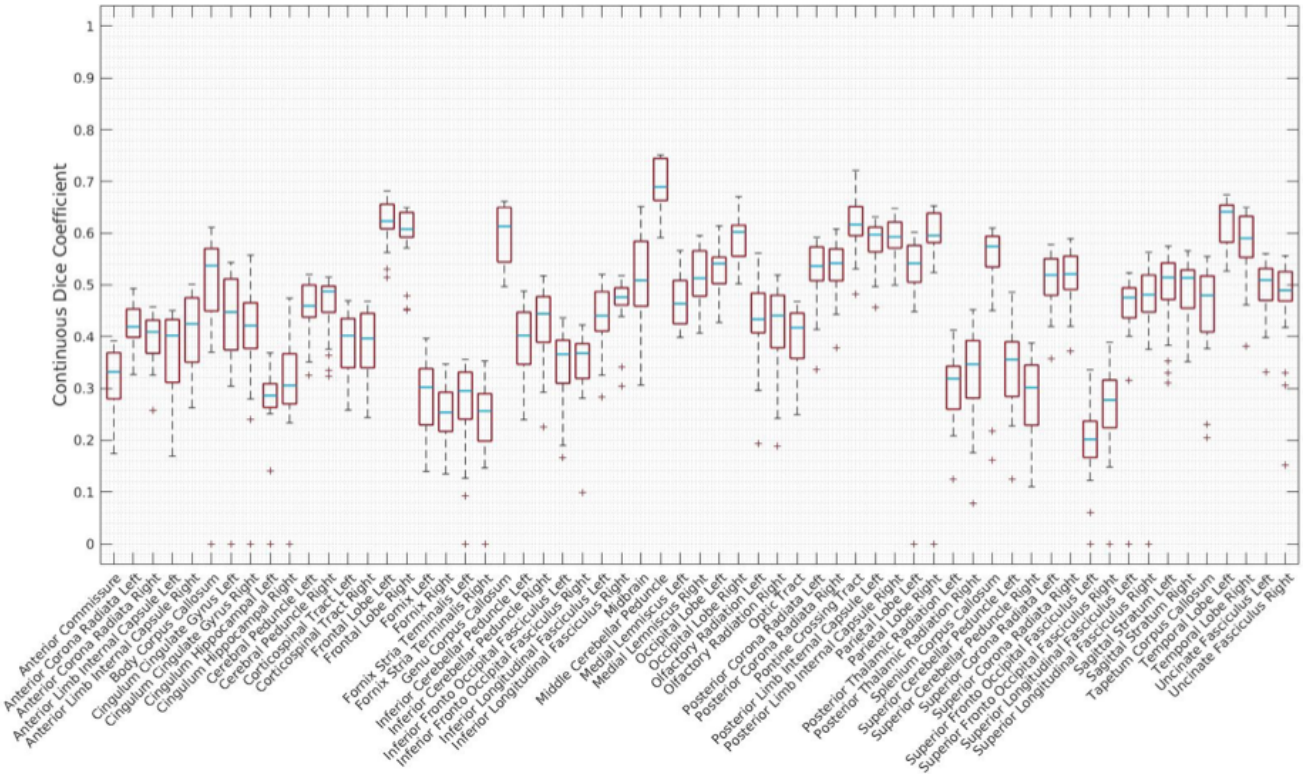

Figure B.11: Inter-subject inter-rater variability for BLSA dataset for all tracts is shown. The reproducibility is evaluated with continuous Dice coefficient. The inter-subject variability shows the anatomical variation in tracts from subject to subject. Low score implies high variation, where high score implies high correlation.

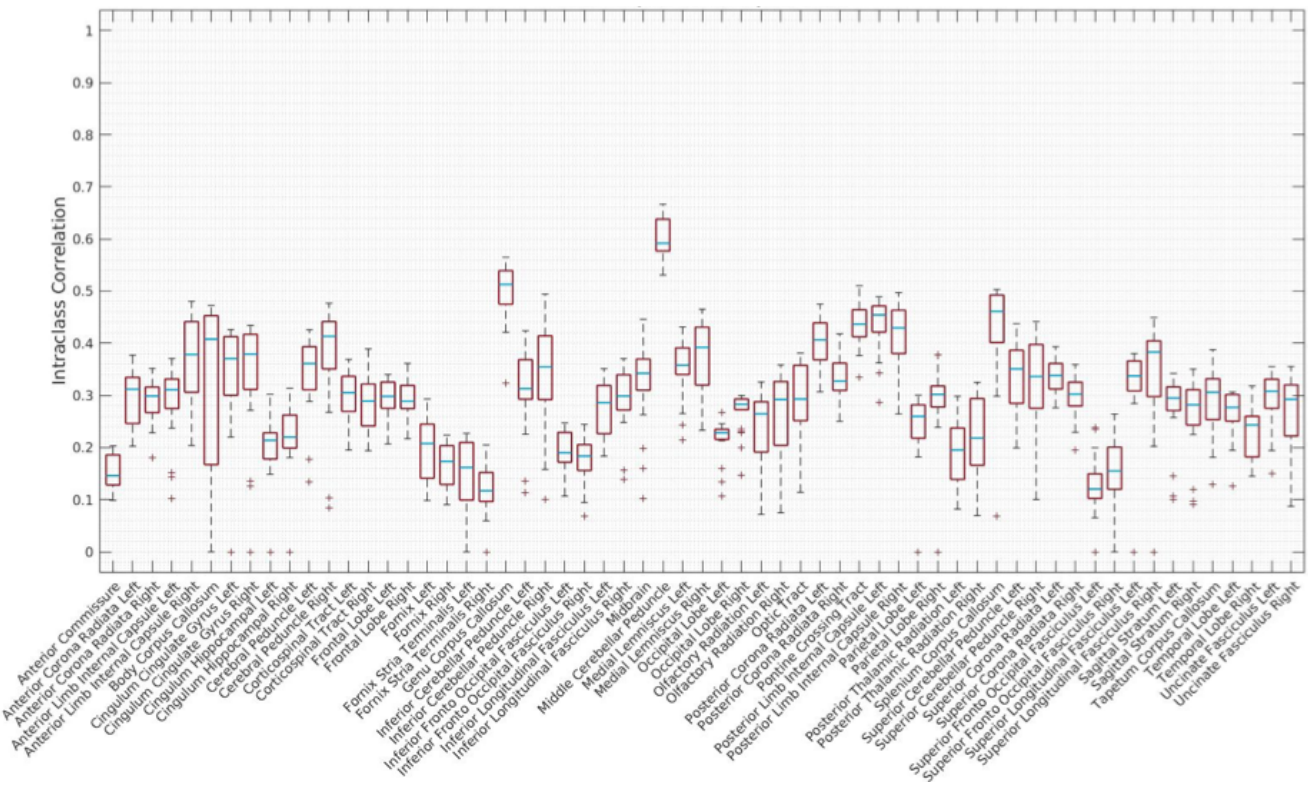

Figure B.12: Inter-subject variability for BLSA dataset for all tracts is shown. The reproducibility is evaluated with intra-class correlation measured. The inter-subject variability shows the anatomical variation in tracts from subject to subject. Low score implies high variation, where high score implies high correlation.

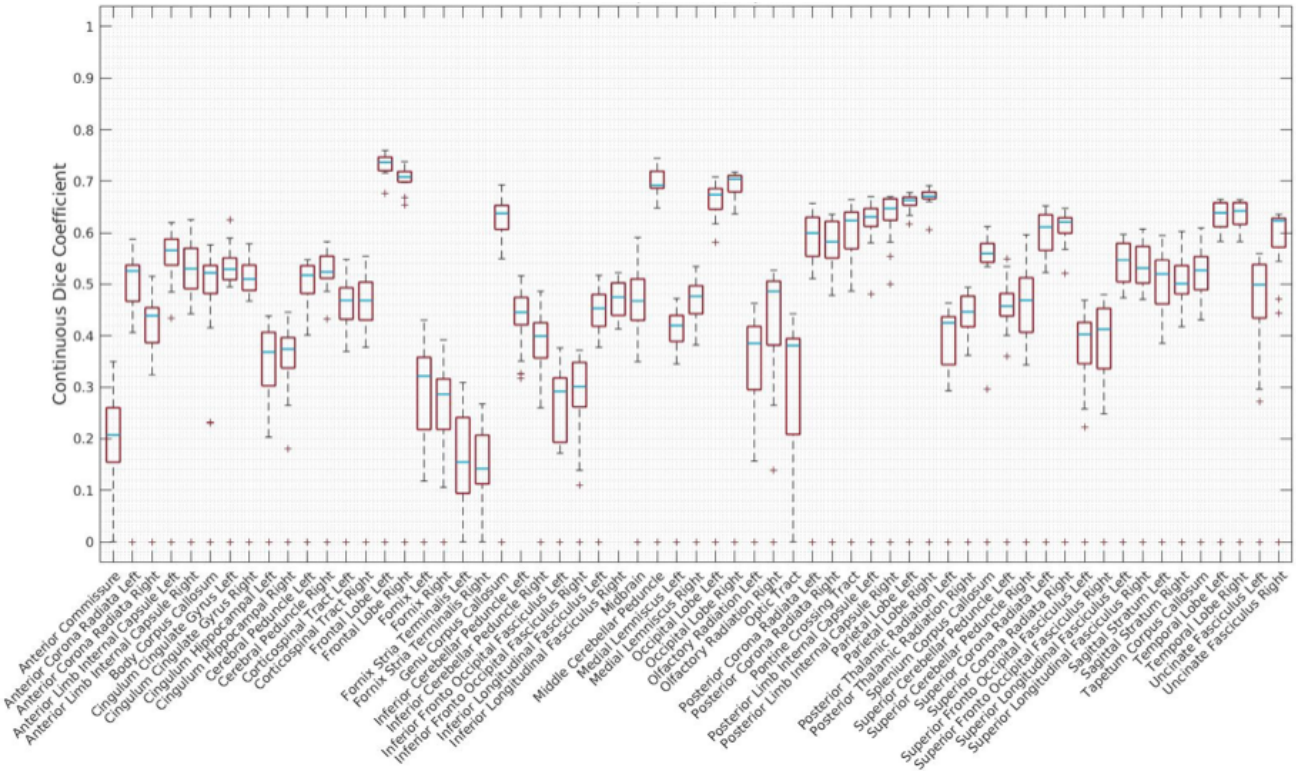

Figure B.13: Inter-subject inter-rater variability for HCP dataset for all tracts is shown. The reproducibility is evaluated with continuous Dice coefficient. The inter-subject variability shows the anatomical variation in tracts from subject to subject. Low score implies high variation, where high score implies high correlation.

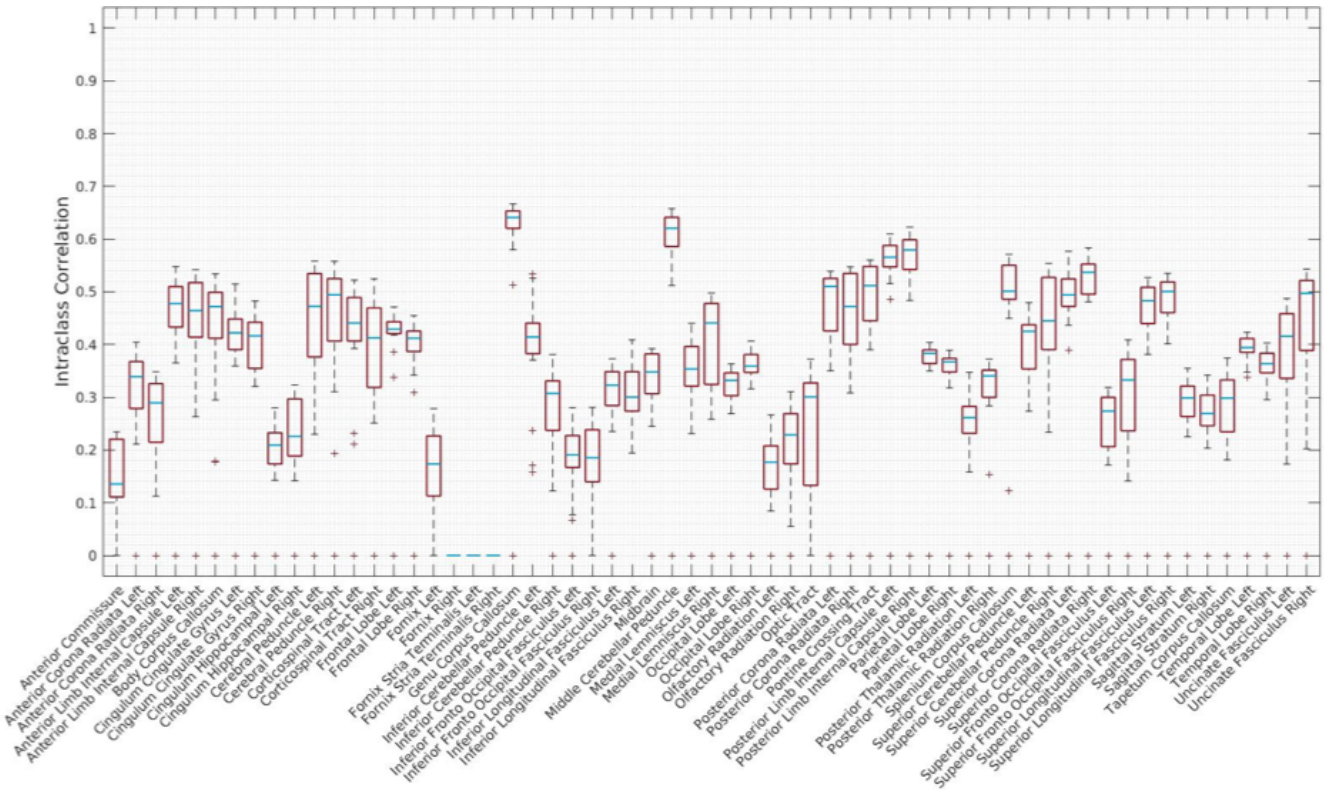

Figure B.14: Inter-subject variability for HCP dataset for all tracts is shown. The reproducibility is evaluated with intra-class correlation measured. The inter-subject variability shows the anatomical variation in tracts from subject to subject. Low score implies high variation, where high score implies high correlation.

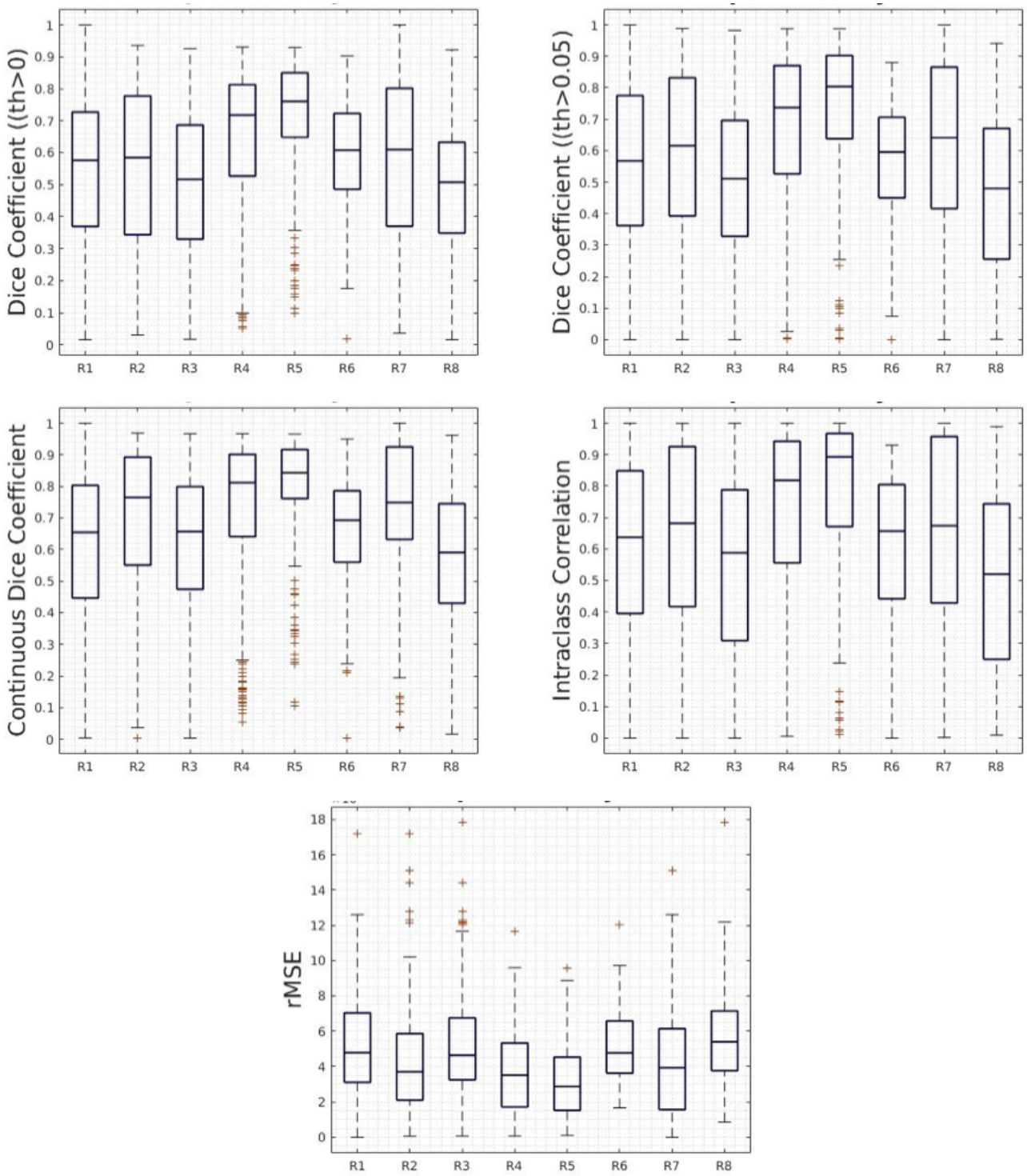

Figure B.15: Rater reproducibility for BLSA dataset is shown for Dice Coefficient with threshold > 0, Dice coefficient with threshold > 0.05, continuous Dice coefficient with threshold > 0.05, intraclass correlation, and root mean squared error (rMSE). The reproducibility was assessed in the intra-subject manner. Raters traced 1-5 subjects depending on their availability.

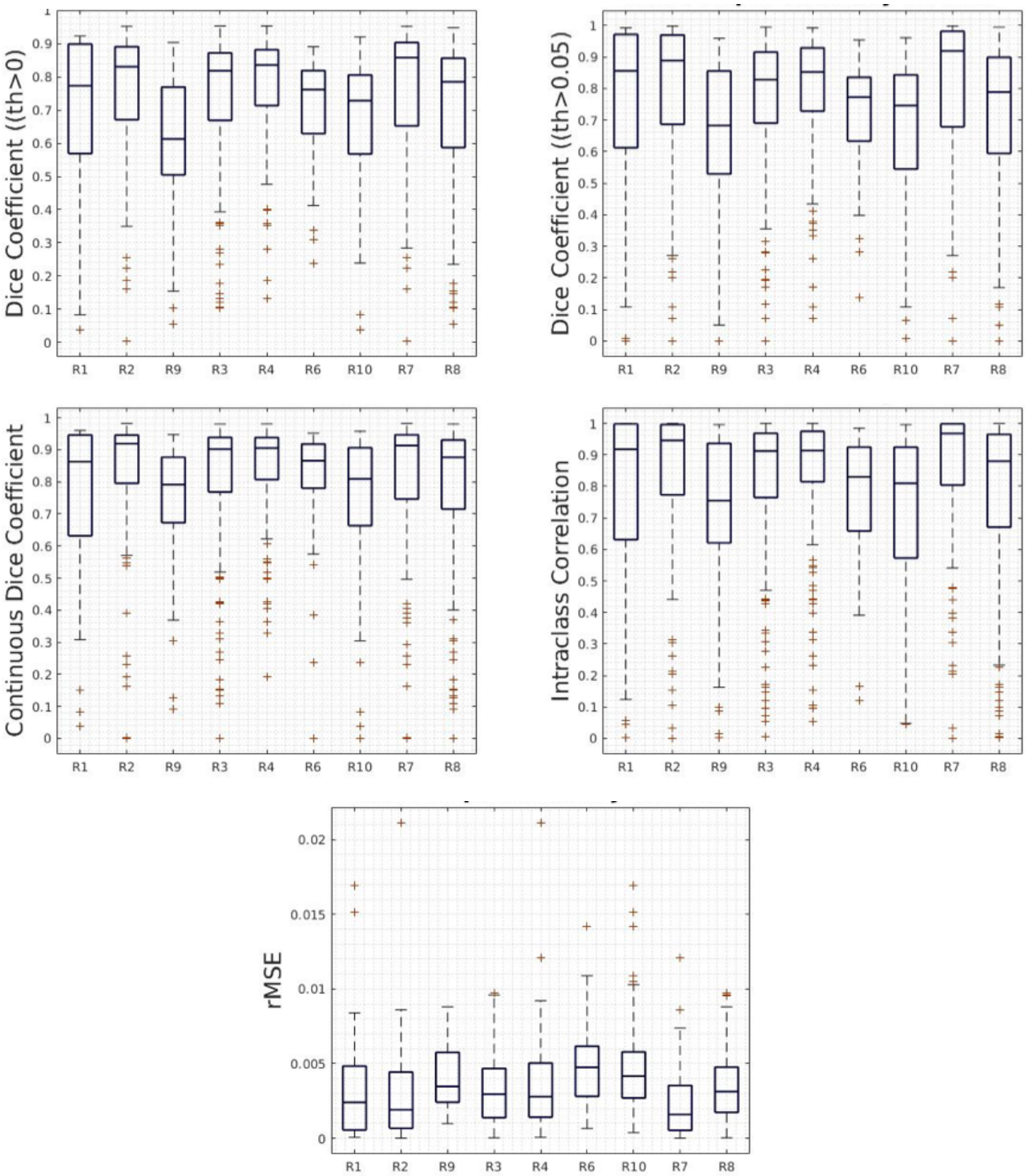

Figure B.16: Rater reproducibility for HCP dataset is shown for Dice Coefficient with threshold > 0, Dice coefficient with threshold > 0.05, continuous Dice coefficient with threshold > 0.05, intraclass correlation, and root mean squared error (rMSE). The reproducibility was assessed in the intra-subject manner. Raters traced 1-5 subjects depending on their availability.

Quantitative Reproducibility Analysis of TractEM dataset	BLSA				HCP			
	ICC		cDICE		ICC		cDICE	
	mean	*std*	*mean*	*std*	*mean*	*std*	*mean*	*std*
anterior commissure	0.6675	0.2933	0.6173	0.1776	0.6779	0.2988	0.6267	0.3324
anterior corona radiata	0.6802	0.1679	0.7380	0.1921	0.6346	0.2548	0.7524	0.1694
anterior limb internal capsule	0.6066	0.2856	0.5984	0.2657	0.8508	0.1852	0.8650	0.1235
body corpus callosum	0.8174	0.2033	0.7562	0.1535	0.8674	0.2252	0.8935	0.0920
cingulum cingulate gyrus	0.7975	0.2136	0.6871	0.2247	0.7789	0.1393	0.8325	0.0685
cingulum hippocampal	0.7617	0.2306	0.6520	0.2914	0.6530	0.2751	0.7246	0.1759
cerebral peduncle	0.6649	0.2622	0.7616	0.1499	0.7782	0.2852	0.8595	0.1240
corticospinal tract	0.6075	0.1871	0.7608	0.1313	0.8659	0.1824	0.8393	0.1088
fornix	0.5182	0.2361	0.5517	0.2741	0.6731	0.2648	0.6150	0.3290
fornix stria-terminalis	0.2433	0.3230	0.3555	0.2891	0.4252	0.4072	0.2697	0.3646
genu corpus callosum	0.8232	0.1934	0.7446	0.2070	0.9604	0.0358	0.9183	0.0455
inferior cerebellar peduncle	0.6466	0.2873	0.6292	0.1819	0.7063	0.2855	0.5821	0.2587
inferior fronto-occipital fasciculus	0.4248	0.3454	0.4920	0.2453	0.6174	0.3622	0.6661	0.2707
inferior longitudinal fasciculus	0.5923	0.2645	0.6853	0.1784	0.7543	0.1418	0.8194	0.0817
midbrain	0.6553	0.3352	0.6893	0.2030	0.7469	0.1833	0.6915	0.1797
middle cerebellar peduncle	0.9110	0.1162	0.8643	0.0997	0.9677	0.0358	0.9288	0.0392
medial lemniscus	0.6925	0.3020	0.7311	0.2087	0.7480	0.2430	0.7426	0.1476
olfactory radiation	0.4786	0.3090	0.6568	0.2340	0.7146	0.3362	0.6947	0.3083
optic tract	0.5182	0.2835	0.4689	0.2318	0.7480	0.3887	0.7688	0.1970
posterior corona radiata	0.7019	0.2078	0.7167	0.1418	0.8774	0.1548	0.8583	0.1106
pontine crossing tract	0.7767	0.2102	0.7747	0.1164	0.9907	0.0138	0.9305	0.0380
posterior limb internal capsule	0.6538	0.1874	0.7297	0.0901	0.9241	0.0946	0.8921	0.0946
posterior thalamic radiation	0.3110	0.2796	0.4248	0.2404	0.7623	0.2444	0.8619	0.0879
splenium corpus callosum	0.6939	0.3095	0.7204	0.2502	0.8549	0.2718	0.8948	0.1044
superior cerebellar peduncle	0.4425	0.2494	0.3823	0.2582	0.8843	0.1585	0.7762	0.1853
superior corona radiata	0.5865	0.2211	0.6879	0.1258	0.9284	0.0782	0.8852	0.0916
superior fronto-occipital fasciculus	0.5200	0.3366	0.5943	0.2653	0.7355	0.3102	0.7412	0.2247
superior longitudinal fasciculus	0.7576	0.1896	0.7671	0.1186	0.8230	0.1698	0.8184	0.1094
sagittal stratum	0.4970	0.2612	0.7164	0.2241	0.7837	0.2301	0.8016	0.1569
tapetum corpus callosum	0.5421	0.2473	0.5166	0.2278	0.6094	0.2563	0.6930	0.1810
uncinate fasciculus	0.5028	0.2147	0.7183	0.1405	0.8902	0.1794	0.8971	0.1215
frontal lobe	0.8625	0.2440	0.8900	0.13742	0.9232	0.0879	0.9356	0.0295
occipital lobe	0.8640	0.2485	0.8984	0.1439	0.9448	0.0435	0.8965	0.0571
parietal lobe	0.9372	0.0929	0.9144	0.0946	0.9316	0.0616	0.9158	0.0336
temporal lobe	0.8938	0.2347	0.9055	0.1082	0.9086	0.0840	0.9082	0.0389

Table B.1: The table describes the manual tractography reproducibility tract by tract. Mean reproducibility and standard deviation for both datasets using ICC and cDICE metrics are provided for readers to view the numerical results along with the provided box plots in Figure B.1-10.